DOCTORAL DISSERTATION

Tidal characteristics in a multi-channel estuary: A Case study on the Ota River estuary

（感潮河川網における潮汐特性：太田川河口域を対象としたケーススタディ）

June 2019

Department of Civil and Environmental Engineering

Graduate School of Engineering

Hiroshima University

DANIAL, MOCHAMMAD MEDDY

Preface

This dissertation is based on observations made in the Ota River estuary, Hiroshima City, Japan. The temporal variation of tidal discharge at a tidal channel junction were collected continuously using fluvial acoustic tomography system (FATS) to investigate the flow division and phase difference between the tidal discharge and water level.

Many people helped me to finish my doctoral program. In the first place, I would like to thank my supervisor Prof. Kiyoshi Kawanishi for his excellent guidance, support, and patience during my doctoral studies. Also, I want to thank Prof. Yasuaki Doi, Prof. Tatsuhiko Uchida, Prof. Akiyoshi Ohashi, and Prof. Ioan Nistor (Ottawa University) for their valuable comments in this dissertation. I am also lucky to be introduced to Prof. Arata Kaneko and Dr. Noriaki Gohda for their sharing knowledge in an acoustic tomography field.

During my doctoral life, I experienced a good research environment in the coastal engineering group at Hiroshima University. I would like to thank Dr. Shinya Nakashita for his help in the coastal laboratory; Dr. Mohamad Basel Al Sawaf for his wonderful support during my field experiment and writing paper. I also thank Junya Kagami, Kaneto, Wakabayashi, Sorimachi and Tanabe, Hiep, Xiao, and Gillang as my colleges.

In this opportunity, I would like to thank the Indonesia government for giving me a scholarship for the doctoral program at Hiroshima University. I also thank Rector of Tanjungpura University and Dean of Engineering Faculty in Pontianak, Indonesia, who permit me to take a doctoral program. Last but not least, I would like to thank my parents for their nonstop support in their entire life for me. I am particularly indebted to my wife Shanty and my daughters Alika and Aliva for allowing me to reach my dreams.

Mochammad Meddy Danial
Hiroshima, Japan

Table of Contents

List of Figures

List of Tables

List of Abbreviations

ADCP	Acoustic Doppler current profiler
ADV	Acoustic Doppler velocimetry
AVM	Acoustic velocity meter
FATS	Fluvial acoustic tomography system
H-ADCP	Horizontal- acoustic Doppler current profiler
RMA 2	Resource modeling associates
SMS	Surface water modelling system
LWS	Low water slack
HWS	High water slack
HW	High water

List of Symbols

A	Wavelet amplitude	m
A_0	Cross-sectional area along the transmission line between two transducers	m^2
c_m	Cross-sectional average sound speed	ms^{-1}
h	Water depth	m
f	Frequency of the acoustic signal	Hz
h_m	Mean water elevation	m
h_{min}	Minimum water depth	m
g	Acceleration due to gravity	ms^{-2}
H	Water Level	m
L	Horizontal distance between the transducers	m
m	Slope of transmission line between two transducers	m
Q	Tidal discharge	m^3s^{-1}
T	Water temperature	°C
S	Salinity	psu
u_m	Cross-sectional average velocity along the transmission line between two transducers	ms^{-1}
v	The cross-sectional average velocity	ms^{-1}
λ	Wavelength of the acoustic signal	m
θ	Angle between the transmission line and the stream line	°
φ	Angle formed by two-crossed paths	°
Z_{B_m}	Elevation of the riverbed along the transmission line	m
t_1	Arrival time at upstream station	s
t_2	Arrival time at downstream station	s
ψ	Discharge asymmetry index	
φ_q	Phase of tidal discharge	°
φ_z	Phase of water level	°
$\Delta\varphi$	Phase difference between the tidal discharge and water level	°
ε	Phase lag	°
s	Scale of wavelet	
k and k'	The time series of two signals	d
δt	Time step	min

M	Length of the time series	d
ψ_o	A normalized wavelet function	
ω_0	The dimensionless frequency of signal	
γ	The dimensionless time	
a_b	Elevation of bottom	m
u,v	Velocities in the Cartesian directions	ms^{-1}
x,y,t	Cartesian coordinates and time	°
ρ	Density of fluid	kgm^{-3}
E	Eddy viscosity coefficient	m^2s^{-1}
n	Manning's roughness n-value	$sm^{-1/3}$
ζ	Empirical wind shear coefficient	
V_a	Wind speed	ms^{-1}
ψ_w	Wind direction	°
ω_r	Speed of earth's angular rotation	rad/s
Φ_l	Local latitude	°

Abstract

The aim of this dissertation is to continuously monitoring of tidal flow/discharge in order to investigate and clarify the phase difference behavior between the tidal discharge and water level at a tidal channel junction. A high-frequency hydro-acoustic instrument is used to collect continuously the velocity, salinity, and tidal discharge. In addition, the 2D velocity distributions at a tidal channel junction are investigated using a 2D numerical model and quantify the magnitude of velocity around the channel junction.

The finding of flow division analysis shows that the temporal variation of subtidal discharge in the western branch is relatively constant, while in the eastern branch the temporal variation of subtidal discharge is relatively varied. The eastern branch has the capability to deliver greater amounts of subtidal discharge, approximately 55–63%, compared with the western branch. The equality of flow division between the eastern and western channels can be observed clearly during the neap tide period.

The finding of phase difference analysis shows that the phase difference in the western is larger than the eastern branch because the western branch is more convergent compared with the eastern branch. Moreover, the temporal variation of phase difference is relatively constant during spring and neap tide.

The finding of salinity analysis at the tidal channel junction shows that the temporal variation of subtidal salinity at the northern branch is smaller than two other branches, irrespective of the tidal range. The temporal variation of subtidal salinity in the eastern and western branches are almost equal without relation to the tidal range.

The finding of velocity analysis at the tidal junction shows that velocity at the eastern branch is higher than that at the western branch, which is consistent with the results of FATS. In addition, the water in the eastern branch flows into the western branch during the flood tide intermittently,

as a result of the transfer of tidal energy from the eastern branch to the western branch. This happens due to the shorter branch of the eastern branch compared to the western branch.

Chapter 1. Introduction

1.1. Study overview

An investigation of hydrodynamics at the tidal channel junction related to the interaction between the tidal wave, upstream river, and the geometrical shape of branches has been carried out by a few researchers. For example, Buschman et al. [1], using numerical model analysis, pointed out that the inequality of subtidal flow division is affected by the geometrical shape of the channel such as depth, length, bed roughness, and river discharge. They also emphasized that the flow division of discharge at a junction cannot merely be estimated from the ratio of the wetted cross-sectional areas of the two branches, because the distribution of flow is also affected by spring and neap tide [1]. Sassi et al. [2], using numerical modeling, highlighted the effect of tide on river flow division, where the inequality increases with the bifurcation order. They also found that during the neap tides, the flow may enter the other branch, leading to an unequal discharge distribution. Zhang et al. [3] found that in general, the tides can modify the river discharge distribution over distributaries in the Yangtze estuary. In their numerical result, they also underline that the fortnightly tidal amplitude also contributes to the inequality of subtidal flow division. Moreover, their findings showed that the effect of tidal range on the inequality of flow division is significant. It is important to note that the previous researchers mentioned above focus on subtidal flow division. Moreover, previous studies mentioned above do not consider the phase difference between the tidal discharge and water level at a tidal channel junction.

The phase difference between the tidal discharge and water level is an important parameter that influences the dynamic behavior of velocity, discharge, salinity, and sedimentation, particularly at a tidal channel junction. The phase difference can be applied as parameter to determine the type of tidal wave and its implication. For instance, the change of phase

difference in an estuarine system can influence the hydrodynamic processes such as amplification and damping of tidal wave [4,5]. For instance, standing wave implies that the tidal range is amplified due to the increased tidal energy as a result of the convergence geometry of the channel. When the phase difference is near quadrature (close to ~90°), the duration asymmetry of water level can induce asymmetries in tidal current magnitude in estuary channel [6]. Moreover, when the water level and velocity covary (the phase difference is 0 degrees), a landward transport of water occurs. Stokes flux is maximal when the phase difference are in phase (the phase difference is 0 degrees) and minimal when the phase difference is 90 degrees [2]. In particular, at a tidal channel junction, the phase difference behaves differently which causes the different subtidal transport of water, sediment and salinity. Thus, the phase difference is very useful to determine the direction of subtidal transport (a landward or seaward transport).

The bulk of the scientific work on the phase difference between the tidal discharge and water level has been focused on single channels. Previous studies, such as Horrevoets et al. [4] investigated the phase difference in a single channel of the estuary and suggested that the river discharge can control the phase difference. They pointed out that the phase difference in the downstream area was mostly constant, whereas in the upstream part of estuary the phase difference was not constant. Moreover, Leonardi et al. [7] investigated the phase difference in the river mouth of the single channel estuary, and they point out that the change in the phase difference is a key factor for the amplification of tidal velocities.

Buschman et al. [1] and Sassi et al. [8] used the numerical model to investigate the flow division at the channel junction without considering to the phase difference between the tidal discharge and water level. A tidal channel junction plays a crucial role in the distribution of discharge, velocity and salinity [9].

Therefore, those phenomena motivated the author to investigate the phase difference between the tidal discharge and water level particularly at a tidal channel junction. Investigating the behavior of phase difference can provides insights into the response of phase difference to channels that connected to a tidal channel junction which is influenced by geometry of channel and river discharge. In addition, to explore the nonstationary behavior of tidal discharge in a complex tidal junction, an acoustic-based instrument with the high-frequency resolution is needed.

1.2.The novelties of the dissertation

The findings of the dissertation are to clarify the phase difference between the tidal discharge and water level as an important parameter that influences the velocity, discharge, salinity, and sedimentation at the tidal channel junction. Previous researchers do not consider the dynamic behavior of phase difference during the spring and neap tide at a channel junction. Also, previous studies could not continuously measure the tidal discharge, velocity and salinity in long-term period and in high-frequency resolution, especially at a tidal junction. They cannot continuously measure discharge using ADCP probably due to two reasons: (i) ADCP are time-consuming to measure discharge and labor-intensive especially in long-term period. Moreover, it is difficult to perform the campaigns during extreme hydrological event (ii) therefore, they use a numerical model and use the ADCP as references for the validation.

This situation motivated the author to observe the variations of phase difference behavior between tidal discharge and water level at a tidal channel junction. The original work of this dissertation is continuously monitoring the tidal flow/discharge behavior to investigate the phase difference between the tidal discharge and water level at channel junction using high-

frequency hydro-acoustic instrument. An innovative hydro-acoustic instrument (FATS) is used, which is capable of measuring discharge continuously in the long-term period.

1.3. Scope of the study

This study focus on the dynamic behavior of the phase difference of tidal discharge and water level in two seaward branches connected to a tidal junction. An innovative hydro-acoustic instrument with high frequency is used to continuously monitoring tidal discharge. The experiment site particularly at three branches connected to a tidal channel junction located in the Ota River estuary.

There are limitations of this study which can be described as follows:

a. The field experiments for investigating the phase difference were carried out during low flow condition, in June and November 2017, where the upstream discharge ranged from 20-40 m^3s^{-1}. In this present study, the author does not consider the seasonal influence on the phase difference in this study.
b. In this study, the boundaries of the investigation only focus on the phase difference of water level and tidal discharge in three branches connected to a tidal junction, and flow division of subtidal discharge between two seaward branches.
c. 2D numerical model (RMA2) was used to investigate 2D velocity distribution at a tidal channel junction. In this 2D numerical model, salinity and density are not included.

1.4. The objectives of the dissertation

The aim of this dissertation is to continuously monitoring of tidal flow/discharge in order to investigate and clarify the phase difference behavior between the tidal discharge and water

level at a tidal channel junction. A high-frequency hydro-acoustic instrument is used to collect continuously the velocity, salinity, and tidal discharge. In addition, the 2D velocity distributions at a tidal channel junction is investigated using a 2D numerical model in order to quantify the magnitude of velocity between two seaward branches connected to a tidal junction.

Thus, the goal of this dissertation can be divide into three sections : (i) observe the tidal flow/discharge behavior at three branches connected to a tidal channel junction investigated using the high-frequency hydro-acoustic instrument, focusing on: flow division behavior and the dynamic of phase difference between the tidal discharge and water level, (ii) investigate the velocity and subtidal salinity at the channel junction, (iii) study the 2D velocity distribution around the junction using 2D numerical model.

1.5. Literature review

1.5.1. Estuaries in general

Worldwide, estuaries are treasured areas with a unique environment and ecology features. Estuaries are also the habitats for human beings, a variety of wildlife and species. However, estuaries area are vulnerable from the threat of sea level rise due to the climate change effect. In addition, a human intervention such as water diversion, dredging, and reclamation can also threaten the estuary environment [10].

There are several definitions of estuary. For example, Pritchard and Cameron in 1967 said that estuary is a semi-enclosed coastal body of water which has a free connection with the open sea and within which sea-water measurably diluted with fresh water derived from land drainage [11]. Perillo in 1995 defined the estuaries almost similar to Pritchard and Cameron [12]. Savenije [13], in 2012, said that estuary could be defined as the transition between two distinct water bodies, i.e., from the river and the sea. On the other hand, from the point of view of

sedimentologist, Dalrymple defines estuaries as a seaward portion of a drowned valley which receives sediment from both fluvial and marine sources, whereas sedimentary facies are influenced by tides, waves, and fluvial processes [14].

According to Savenije [13], estuaries can be affected by the main drivers, i.e., the tide, the upstream discharge, the wave, the lateral sediment transport, the density difference, and the climate. Similarly, Dalrymple also pointed out that estuaries are controlled by the tides, river outflow, waves and their variation in time [15]. From these drivers, the tide and the river discharge are the two most significant factor in determining estuary shape [13,15].

Savenije [13] classified the estuaries into the five categories: (i) shape, (ii) tidal influence, (iii) river influence, (iv) geology, (v) salinity. Each category of the estuary can be explained as follows.

a) Classification by shape, estuaries can be distinguished, as follows:
   - Prismatic: Estuaries with the shape of channel banks are parallel and constant cross-section. This type of estuary is a man-made environment.
   - Delta: A prismatic estuary with a small tidal influence compared to the river discharge.
   - Funnel or trumpet shape: The channel banks converge in the upstream direction.
   - Fjords and Rias: Fjords is formed by the submerged valley as a result of glaciers that eroded the underlying rock. Rias is formed due to the submergence of river valleys. Their branches are irregular banks.
   - Bays: Semi-enclosed bodies with no significant input of discharge from upstream area.

b) Classification by tidal influence:
   - Ideal estuary: An estuary where the amount of energy per unit width gained by the convergence of the banks is equal with the energy per unit width lost by friction. In an ideal estuary, the tidal range is constant along the estuary channels.

- Amplified estuary: An estuary with the tidal range increases in the upstream direction because the convergence is stronger than friction. The dampening process occurs due to the river discharge which increases the friction.
- Damped estuary: An estuary where friction is stronger than convergence. Tidal damping occurs in estuaries with a small convergence length.

c) Classification by river influence:
   - Riverine estuary: An estuary which is dominated by the river flow.
   - Marine estuary: An estuary which is dominated by the sea.

d) Classification by geology:
   - Fixed bed estuary: An estuary with a fixed bed as a result of an older geological period.
   - Short alluvial estuary: An estuary which is located in a submerged valley or fjord. These estuaries are alluvial which has not yet reached a stage of morphological equilibrium.
   - Long alluvial or coastal plain estuary: A fully alluvial estuary consisting of sediments deposited from the river and the sea. It has an exponentially varying cross-section and almost no bottom slope.

e) Classification by salinity. Estuaries can be classified based on salinity behavior, as follows:
   - Positive or normal estuaries: These estuaries have a salinity profile which decreases gradually in the upstream direction.
   - Negative or hypersalines estuaries: The salinity profile increases in the upstream direction. These estuaries usually have a shallow geometry, the evaporation exceeds the rainfall, and the amount of freshwater upstream is too small to balance the salinity.

Besides the mentioned above, the classifications of estuaries can be categorized by the tidal range or amplitude of the tidal wave. Davies [16] proposed a classification of the estuaries according to the tidal range, i.e., (i) microtidal, it has a tidal range less than 2 m; (ii) mesotidal,

it has a tidal range from 2-4 m; (ii) macrotidal, it has a tidal range from 4-6 m, and (iv) hypertidal, it has a tidal range greater than 6 m.

Similarly, Nichols and Biggs [17] proposed the three types of estuaries based on the tidal amplitude which is influenced by geometric characteristic, i.e., (i) the hypersynchronous, it means the effect of convergence is stronger than effect of friction, and as a consequence, the tidal amplitude and tidal currents increase in the upstream direction; (ii) hyposynchronous, it means the friction exceeds the convergence, and as a result, the amplitude and tidal current decrease in the upstream channel; (iii) the synchronous, it means the convergence and the friction is balance and the tidal range or tidal amplitude is constant along the estuary.

Savenije [13] proposes to classify estuaries based on the combination of estuarine characteristic, as shown in Table 1.1.

Table 1.1. Classification of estuaries based on a combination of estuarine characteristic

Type	Shape	Tidal wave type	River influence	Geology	Salinity	Estuarine Richardson number
1	Bay	Standing wave	No river discharge	Compound type	Sea salinity	Zero
2	Ria	Mixed wave	Small river discharge	Drowned drainage system	High salinity, often hypersaline	Small
3	Fjord	Mixed wave	Modest river discharge	Drowned glacier valley	Partially mixed to stratified	High
4	Funnel	Mixed wave, large tidal range	Seasonal river discharge	Alluvial in coastal plain	Well-mixed	Low
5	Delta	Mixed wave; small/ large tidal range	Seasonal river discharge	Alluvial in coastal plain	Partially mixed to well-mixed	Medium
6	Infinite prismatic channel	Progressive wave	Seasonal river discharge	Man-made	Partially mixed to stratified	High

1.5.2. Tidal dynamics in estuarine

The tide is a periodic upward and downward motion of the water surface. Moreover, the tide is classified as a type of long wave which has a long period ranged from 12.5 to 24 hrs. In addition, there are four types of a tidal regime based on the period of a tidal cycle, i.e., semidiurnal tide, diurnal tide, mixed with the predominantly semidiurnal tide, and mixed with the predominantly diurnal tide. On the other hand, river discharge is not periodic. It varies over time but relatively constant and usually characterized by the seasonal condition. Moreover, river discharge increases due to rainfall condition.

The tidal motion is influenced by the spring and neap tide. The spring tide occurs when the Moon, the Earth, and the Sun located at the same side, i.e., during a full and new moon, whereas the neap tide occurs when the Moon position perpendicular to the Sun, i.e., during near Moon first quarter and Moon last quarter.

Tides and river discharge can affect each other [4,7,18,19]. For example, river discharge can strongly affect tidal propagation by attenuating tidal energy, reducing tidal amplitude, decreasing tidal range, and delaying wave propagation. On the contrary, tides can propagate far in the upstream direction from the river mouth and hamper river discharge. River-tide interaction can cause a variation of water level and flow during spring and neap tide [1]. In addition, river-tide interaction can create a subtidal water level which increases in the landward direction [18,20].

The tide which propagates in the upstream direction is also distorted by several factors, such as shallow water friction and shape of topography (convergence in river width and river depth) [21,22]. In addition, Alebregtse and Swart [23] stated that the river discharge and the geometry of channels can affect the tides and net water transport in an estuarine network.

There are three types of tidal distortion which represents the characteristic of the estuary, i.e., dampening, amplification and constant/ideal [13,24]. Moreover, tidal motion can behave

as a progressive wave, standing wave, and mixing wave. The progressive wave type occurs in the deep and wide channel with the phase difference between tidal discharge and water level at 0°, whereas standing wave occurs in a shallow and narrow channel with a phase difference at 90°. Likewise, the mixed wave type usually occurs in the most estuary with the phase difference between 0°-90° [10,13].

The characteristics of the tidal channel are different between the upstream side and downstream side. On the upstream side, the tidal channel is influenced by fresh water, whereas the downstream side is an estuary and affected by saltwater or brackish water. The interaction between saltwater and fresh discharge from the land side results in a mixing and stratification process in estuaries [25].

Leonardi et al. [7] revealed that the interaction between tide and river discharge at the delta estuary is dynamic, i.e., when the tidal discharge is higher than the river discharge, the tidal damping increased and the amplitude of tidal velocities decreases. In contrast, when the river discharge is high, the tidal motion effect is negligible, resulting in the transformation from bidirectional to unidirectional exists, which changes characteristic from tidally dominated estuary to river-dominated estuary. As a consequence, the phase difference between water level and tidal discharge also changes from standing wave type (phase difference = 90°) to progressive wave type (phase difference = 0°).

1.5.3. Tidal multi-channel network

Estuaries around the world are commonly characterized by the multi-channel network and junctions [23]. The tidal channel in estuaries often splits into several channels that form a multi-channel network [23]. A multi-channel network at least has two branches [26]. Furthermore, the branching channel network in estuaries also tends to form an asymmetrical bifurcation as

shown in Figure 1.1. [27]. The configuration of multi-channel of estuaries, such as widths, depths, and length of channels, are usually not the same [1,28].

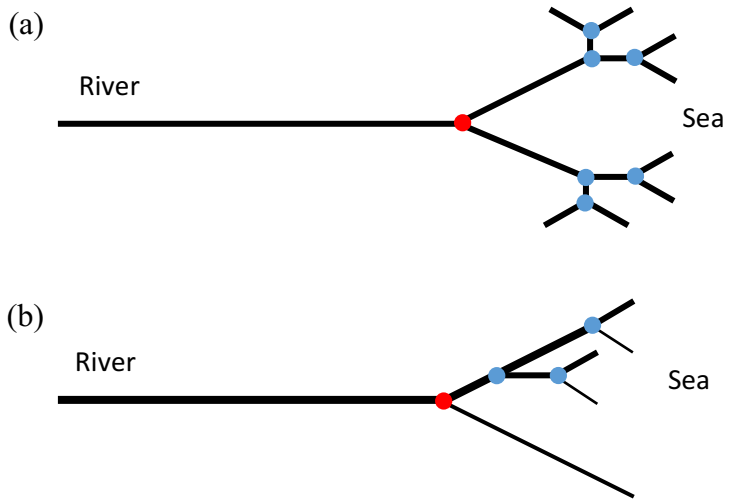

Figure 1.1. (a) Symmetric bifurcation channel network (b) asymmetric bifurcation channel network. The red and blue circle denote apex junction and junctions, respectively.

The behavior of streamflow in a multi-channel network is complicated by tidal motion. For example, when tidal motion propagates at a channel junction consisting of three branches, the tidal energy can propagate in two directions and affect each other. As a result, the tidal discharge and phase difference in three tidal channels are not the same [1].

Buschman et al. [1] pointed out that in the tidal junction, the division of discharge cannot merely be estimated from the ratio of wetted cross-sectional areas between the two branches. However, tides can also affect the distribution of river discharge at channel or branch connected to a junction. Moreover, the tidal range can influence the flow division at a junction [1].

In the multi-channel network, the influence of tide on the division of discharge at the junction between flood tide and ebb tide is different. Similarly, the behavior of flow division at the junction also differs between the spring and neap tide. Based on the previous work of Buschman et al. [1], as long as there are differences of the geometric shape of branch (asymmetries in the depth, the width and the length of branch) between two branches, the behavior of flow division at the junction is more unequal during the spring tide than that of the

neap tide. Buschman et al. [9] also pointed out that differences in geometry shape between the connecting channels cause strong differences in amplitude and phase of the tidal flow at the channel junction.

The characteristic of flow in estuarine is unsteady, bidirectional, and more complicated at the tidal junction, particularly. Therefore, the division of streamflow, salinity, and sediment at the tidal junction or bifurcation depend on several factors such as the geometrical shape of a branch, tidal motion, spring-neap tide, and flood-ebb tide. Thus, a multi-channel network plays an important role in controlling the division of streamflow, salinity and sediment [9,18].

1.6. Study area

The Ota River estuary is a small-scale estuary with a multi-channel network that connects to the Hiroshima Bay, located in Hiroshima City, Japan. Historically, the channel network of Ota River was formed on the Ota River delta [29]. The Ota River has important environmental qualities, and the downstream area is also known as a habitat of many creatures, particularly oysters.

As shown in Figure 1.2a, the Ota river has an apex junction with an asymmetric branch pattern and a North-South oriented branch. It consists of the Ota River floodway (the Westernmost branch), Tenma River (western branch), Kyu Ota River (eastern branch), the Motoyasu (southern branch), and Enko Rivers (the Easternmost branch) as the five main branches. The channel network of the Ota River estuary is characterized as a mixed-semidiurnal tide and mesotidal with a tidal range varying from 2 to 4 m. The catchment area of the Ota River is approximately 1710 km^2. The freshwater discharge that is monitored at the Yaguchi gauging station mostly varies between 20 to 50 m^3s^{-1} during the low-flow condition except during periods of heavy rainfall.

There are two sluice gates at the Ota River floodway positioned near the first bifurcation channel (see figure 1.2a). The sluice gates of Gion consist of a movable weir with three gates that only open 10% during normal operation; the Oshiba gates consist of a movable weir with three gates that are completely open throughout the year.

The studied junction is in the middle part of the Ota River network channel, approximately 2.5 km downstream from the main bifurcation channel (apex junction) and approximately 5.8 km from the river mouth, as shown in Figure 1.2b. The tidal junction consists of three branches: the northern branch (upstream Kyu Ota River), the eastern branch (downstream Kyu Ota River), and the western branch (Tenma River). As an estuary system with a multi-channel network, the saltwater intrusion in the Ota River can reach 11.5 km upstream from the river mouth. The bed materials of the channel network mostly consist of sand containing littler silt and clay.

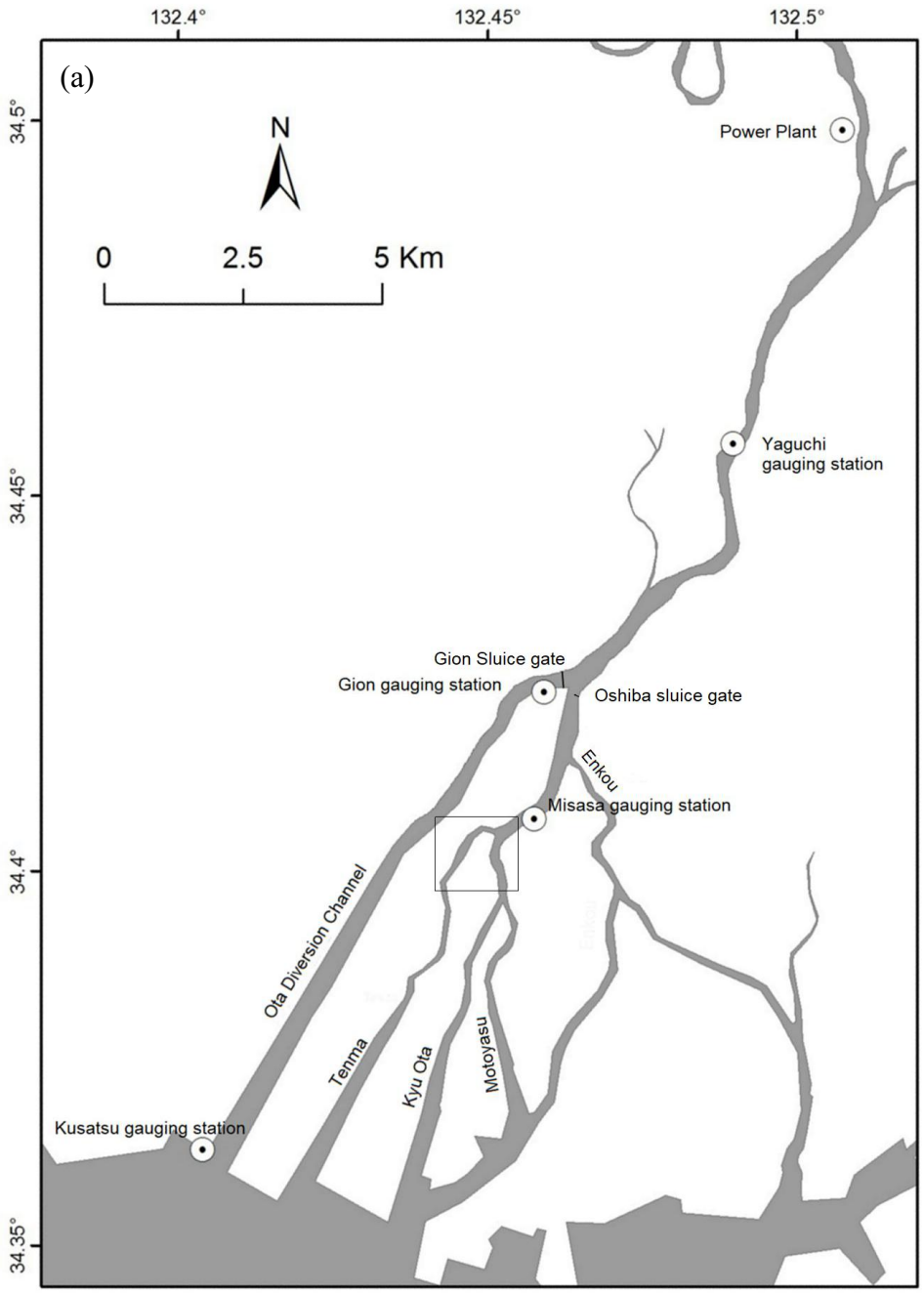
(a)
132.4°
132.45°
132.5°
34.5°
34.45°
34.4°
34.35°
N
0
2.5
5 Km
Power Plant
Yaguchi
gauging station
Gion Sluice gate
Gion gauging station
Oshiba sluice gate
Enkou
Misasa gauging station
Ota Diversion Channel
Tenma
Kyu Ota
Motoyasu
Kusatsu gauging station

Figure 1.2 (a) Ota river channel network map. The black box denotes the study area. (b) Observation site at the tidal channel junction, consisting of the eastern, western, and northern branches.

1.7. Dissertation organization

This dissertation consists of six chapters:

a. Chapter one contains the introduction, describing an overview of general estuarine physics, river-tide interaction, multi-channel network, overview, the novelties of the study, the objective of the dissertation, and study area.

b. Chapter two presents an overview of an acoustic-based instrument, measurement principle of fluvial acoustic tomography system (FATS), determining of flow angle in FATS measurement, discharge acquisition by FATS.
c. Chapter three presents the temporal variation of tidal discharge at the tidal channel junction using acoustic tomography instrument, bathymetry survey at a tidal junction, application index velocity method and two-crossed paths of FATS for discharge measurement, discharge validation, analysis of flow division between two seaward branches using discharge asymmetry index, investigation the influence of spring and neap tide on the flow division.
d. Chapter four presents the temporal variation of the phase difference between the tidal discharge and water level using wavelet method between three branches connected to the tidal channel junction, an overview of wavelet method for tidal analysis in an estuary, and investigate the dominant factor of the phase difference behavior between two seaward branches.
e. Chapter five consists of two works, i.e., investigating the tidal velocity and subtidal salinity using FATS and investigating the 2D velocity distribution at the channel junction using a 2D numerical model.
f. Chapter six presents conclusions and future works.

Chapter 2. Acoustic-based instruments for hydraulics and coastal research

2.1. Acoustic-based instruments

Currently, various flow measurement device based on acoustic [30–35] are significantly improving the capability to measure discharge and velocity of rivers at higher spatial resolutions. The examples of types of acoustic-based instrument, i.e., acoustic Doppler velocimetry (ADV), acoustic velocity meter (AVM), acoustic Doppler velocity profilers (ADCP), and Horizontal acoustic Doppler current profilers (H-ADCPs).

Those kinds of instruments are much more efficient than the traditional and mechanical instrument because they can measure velocities faster and can cover a larger area [36]. In addition, such advance instrumentations can also reduce the costs and effort, and certain instruments can be used to safely measure velocity and discharge during extreme hydrological events.

Nevertheless, there are still limitations in the utilization of those instruments. For example, an acoustic-based technique such as horizontal acoustic Doppler current profilers (H-ADCPs) is not capable of measuring velocity distributions over the entire cross-section [37] in a shallow and wider river [35] owing to their fixed positions and the limitation of the length distance of river width. Similarly, moving-boat ADCP cannot measure the discharge through an entire water column; it has unmeasured areas near water surface [38] and bottom [39]. Moreover, the measurement of moving-boat ADCP increased risks during flood events or in extreme hydrological conditions [40]. Another acoustical type such as acoustic velocity meter (AVM) based on time-of-travel method also have disadvantages [41], including the facts that (i) conventional time-of-travel AVM assume straight-line propagation in the estimation of representative index velocities, (ii) the calibration error is found to be a fundamental source of

error in discharge estimation, and (iii) the refraction of the acoustic path under stratified conditions causes unacceptable uncertainties in the determination of the streamflow.

2.2. Measurement principles of FATS

Fluvial acoustic tomography system (FATS), developed by Hiroshima University, is a type of acoustical based measurement device that is used to measure the hydraulical parameters such as velocity, discharge, temperature, and salinity. The measurement principle of the FATS is similar to that of an Acoustic Velocity Meter (AVM) that utilize the time-of-travel method where sound waves are transmitted along a diagonal line in both directions (between two transducers) and the travel time is calculated in each direction. In addition, the time-of-travel method is used to determine a velocity between two points of transducers. The method works on the principle that the upstream travel time of sound between two transducers is longer than the downstream travel time, and this difference can be measured accurately [32].

In contrast to AVM, the sound pulses of the FATS are simultaneously transmitted from omnidirectional transducers every 30 s at times that are synchronized with a GPS clock with an accurate timing pulse at a frequency of 1 Hz. Thus, FATS is capable of measuring the cross-sectional averaged flow velocity and streamflow continuously in the long term and collecting data every 30 s.

The limitation of minimum water depth using FATS depends on the acoustical wavelength. The minimum water depth of FATS measurements can be found using the following criteria of wave propagation: $h_{min} > 10\ \lambda$, where h_{min} is the minimum water depth and λ is the wavelength. The wavelength of the acoustic signal can be calculated using $\lambda = c_m/f$, where c_m and f is the sound speed and frequency, respectively; for $c_m = 1450$ ms^{-1} and $f = 30$ kHz, the wavelength λ is 0.048 m. Hence, the minimum water depth can be estimated as $h_{min} \sim 0.5$ m. Thus, FATS can operate in shallow conditions at the minimum water depth of 0.5 m and can operate under a large aspect ratio (width-to-depth) [35].

FATS instrument is easier and more practical to operate it compared to ADCP especially in long-term period. Moreover, FATS can still be operated during extreme hydrological event. In contrast, ADCP are time-consuming to measure discharge, labor-intensive in the long term period, and it is difficult to perform the campaigns during extreme hydrological event.

The FATS can manage various hydrological and hydrodynamic issues, and therefore can be considered as an innovative technology in the field of water resources. Some of advanced applications of FATS were demonstrated in the previous works [35,42,43]. Moreover, FATS measurement is reliable for acquiring velocity and discharge with the largest possible error of FATS performance ranged from 14−19% [35,43].

Illustration of deployment the FATS instruments in the river can be seen in Figure 2.1.

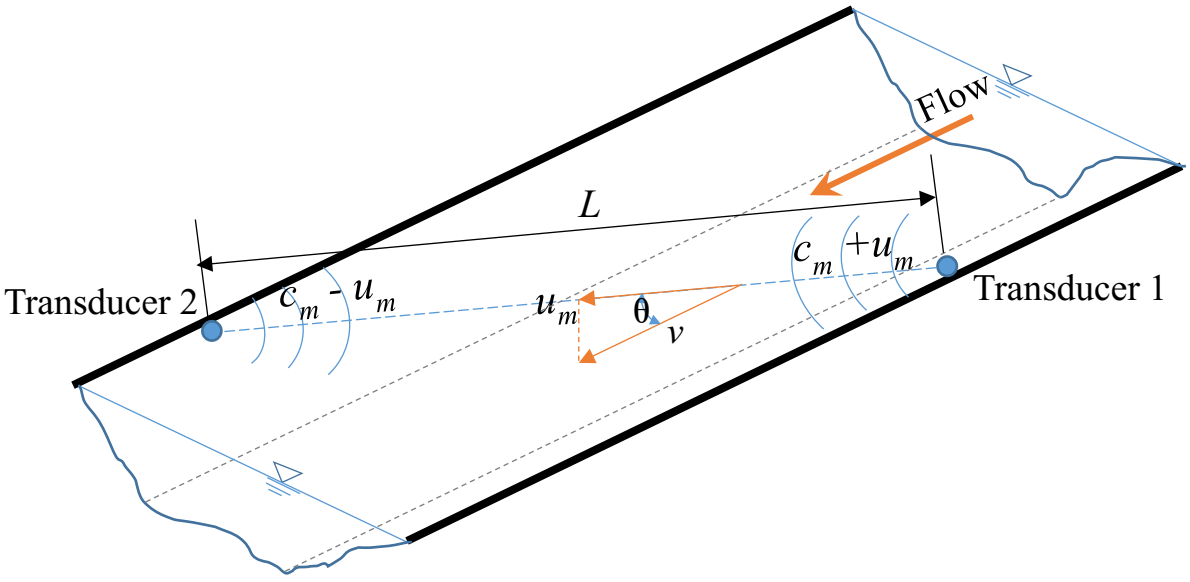

Figure 2.1. Illustration for deploying FATS instrument in the river using two transducers. Transducer 1 and 2 represent upstream and downstream position.

The travel times t_1 and t_2 for the forward and reverse directions are calculated using the following formulae

$$t_1 = \frac{L}{c_m + u_m} \tag{2.1}$$

and

$$t_2 = \frac{L}{c_m - u_m} \tag{2.2}$$

where L is the horizontal distance between the transducers, c_m is the sound speed, and u_m is the cross-sectional average velocity along the transmission lines. From equation 2.1 and 2.2, c_m and u_m are respectively expressed as

$$c_m = \frac{L}{t_m} \text{ and } u_m = \frac{{c_m}^2}{2L}\ \Delta t \tag{2.3}$$

where $t_m = \frac{t_1+t_2}{2}$ and $\Delta t = t_1 - t_2$.

The cross-sectional average velocity (v) in the direction of the streamflow can be estimated using the following equation

$$v = u_m / \cos\theta \tag{2.4}$$

where θ is the angle between the transmission line and streamflow direction. Thus, the discharge of FATS (Q) can be computed by

$$Q = A_0(h) u_m \tan\theta \tag{2.5}$$

where A_0 is the cross-sectional area along the transmission line, and h is water level.

2.2.1. Determining flow angle of FATS measurement

FATS and AVM measurement require the flow angle information to estimate the velocity and discharge [32,35,41]. If the horizontal angle of streamflow in a channel is constant, the one diagonal line of the acoustic path is likely adequate to estimate the streamflow accurately. Nevertheless, varies of flow angle over time and space can induce a considerable error in determining streamflow, particularly in a tidal channel and in such a complex flow field

condition [42]. Moreover, bidirectional flow and such irregular channel bathymetry can generate the fluctuation of streamflow direction [42].

There are various methods to determine flow angle using FATS instrument. In the previous works, Kawanisi et al. [27,28,36,37] have proposed three methods for estimating streamflow in a mountainous river, i.e., nonlinear regression, two crossing paths, and index velocity rating. All results have shown that FATS was reliable with the relative residuals between the FATS and ADCP/Rating Curve (RC) are within 1-20%. Preliminary work of using two crossed paths in the tidal channel estuary has been conducted by Razaz et al. [42] to measure velocity during half of the tide cycle. The experiment was located at the downstream branch of the bifurcation channel. Recently, another effort of using two crossed acoustic paths has been developed by Bahreinimotlagh et al. [43] that is combined with a new formula based on the continuity equation to measure flow angle and discharge in the mountainous river with the unidirectional flow.

2.2.2. Acquisition of streamflow data using the single transmission line

In the case of discharge measurement using single paths of FATS, equation 2.5 was used to calculate discharge. The deployment setting similar to the illustration shown in Figure 2.1. To obtain the cross-sectional area (A_0), water level data and a topographical profile of the channel bed along the transmission line should be measured. The moving-boat ADCP measurement was used to collect the cross-sectional profile of the bed level (Z_{B_m}) along the transmission lines. The vertical resolution of the ADCP measurement was $\pm$0.01 m. The water-level loggers (Hobo U20-001-01-Ti, Onset Co.) were installed at the transducer to measure water level every 10 min. The total error of water level was $\pm$0.01 m. Before obtaining water level estimates, the measured pressure values should be corrected by the atmospheric pressure, as recorded by the barometer deployed on the riverbank. Water level data were acquired from

the post-processing of the water pressure and barometric data as parameter inputs to the software program Hoboware Pro [45,46].

2.2.3. Acquisition of streamflow data using the two-crossing transmission lines

In the case of discharge measurement using two-crossing paths of FATS, equation 2.5 was modified in the term of the continuous equation, where the streamflow obtained from the transmission line of M_1-M_2 and M_3-M_4 should be equal. The continuity equation for calculating streamflow using two crossing acoustical paths is given as

$$Q_{M_1-M_2} = Q_{M_3-M_4} \tag{2.6}$$

$$A_1(h_1)u_{m\,M_1-M_2} \tan\theta_1 = A_2(h_2)u_{m\,M_3-M_4} \tan\theta_2 \tag{2.7}$$

where A_1 and A_2 are the cross-sectional area along the transmission lines of M_1-M_2 and M_3-M_4, respectively; θ_1 denotes the angle between the transmission line M_1-M_2 and the streamflow; similarly, θ_2 denote the angle between the transmission line of M_3-M_4 and the streamflow (See Figure 2.2).

As shown in Figure 2.2, the angle (φ) formed by two-crossed paths can be computed by a simple equation as follows

$$\varphi = \tan^{-1}\left[\frac{m_{M_1M_2} - m_{M_3M_4}}{1 + (m_{M_1M_2}\, x\, m_{M_3M_4})}\right] \tag{2.8}$$

where $m_{M_1M_2}$ is the slope of transmission line between two transducers (M_1-M_2) and similarly $m_{M_3M_4}$ is the slope of the transmission line between two transducers (M_3-M_4). To calculate θ_1, the author uses equation 2.7 as follows

$$\theta_1 = \tan^{-1}\left[\frac{u_{mM_3M_4}\, A_2}{u_{mM_1M_2}\, A_1} \tan\theta_2\right] \tag{2.9}$$

substituting $\theta_2 = \varphi - \theta_1$, the equation 2.9 become

$$\theta_1 = \tan^{-1}\left[\frac{u_{mM_3M_4}\,A_2}{u_{mM_1M_2}\,A_1}\tan[\varphi - \theta_1]\right] \tag{2.10}$$

It is important to note that equation 2.10 is an implicit equation; hence, it can be solved by using iteration method.

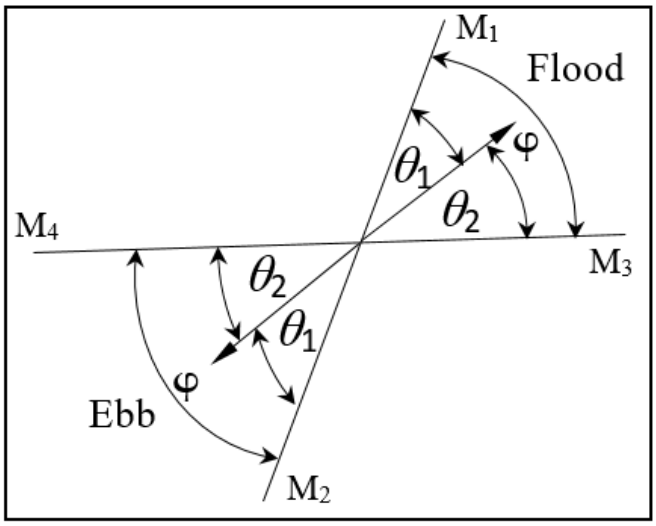

Figure 2.2. Illustration for deploying FATS instrument using two crossing transmission lines with four transducers in the tidal channel. The M1-M2 and M3-M4 represent transducers position.

2.3. Validation method for FATS measurement

Moving-boat ADCP (Teledyne RDI 1200 kHz Workhorse and StreamPro) was used as a set of reference discharge data and flow direction for evaluating the results of FATS measurement. There are two types for ADCP campaign, i.e., along the transmission line between two transducers and along the bridge near the transducers. ADCP campaign was conducted approximately every 5-10 min to collect the data, depending on the distance of the transmission length or the bridge length. Each discharge was estimated from two transects. ADCP discharges can be obtained using WinRiver II software in which each of the bad bin ensembles parts did not exceed 2%, while bad ensembles did not exceed 3% in each transect.

Chapter 3. Tidal discharge at a channel junction

3.1. Introduction and purpose

One of the most important features in a tidal channel network is the bifurcations, which are mostly located in the middle section of a delta. In the tidal channel network, there are many branches/ junctions that are commonly bifurcated asymmetrically [28]. Due to the different geometrical shape of branches, the behavioral pattern and magnitude of discharge in the first branch are different from the second branch. In a tidal channel junction where there are three channels connected, the tides that propagate upstream in the channels affect each other, and the tidal energy can propagate in two directions. As a result, the magnitude of discharge and its phases in three tidal channels are not similar [1,8].

An investigation of hydrodynamics at the tidal channel junction related to the interaction between the tidal wave, upstream river, and the geometrical shape of branches has been carried out by a few researchers. For instance, Buschman et al. [1], using numerical model analysis, pointed out that the inequality of subtidal flow division is affected by the geometrical shape of the channel such as depth, length, bed roughness, and river discharge. They also emphasized that the flow division of discharge that connects to a junction cannot merely be estimated from the ratio of the wetted cross-sectional areas of the two branches, because the distribution of flow is also affected by spring and neap tide [1]. Sassi et al. [8], using numerical modeling, highlighted the influence of tide on river flow division where the inequality increases with the bifurcation order. They also found that during the neap tides, the flow may enter the other branch, leading to an unequal discharge distribution. Zhang et al. [3] found that in general, the tides can adjust the river discharge distribution over distributaries in the Yangtze estuary. In their numerical result, they also underline that the fortnightly tidal amplitude also gives a

contribution to the inequality of subtidal flow division. Moreover, his findings showed that the effect of tidal range on the inequality of flow division is significant.

In this chapter, the temporal variation of flow division between the two seaward branches (eastern and western branches) that connected to the junction during neap and spring tide will be investigated. The purpose of this chapter is to quantify the flow division between the eastern branch and western branch using discharge asymmetry index and to investigate the influence of spring and neap tide on the flow division between two seaward branches.

3.2. Acquisition of FATS data

The tidal discharge data were measured continuously using FATS from 8 to 20 June 2017 and 9 to 29 June 2017 for the western and eastern branches, respectively (see Table 3.1). Two pairs of FAT systems were deployed at the western and eastern branches located near a tidal junction as shown in Figure 3.1. The acoustic pulses (central frequency: 30 and 53 kHz) were transmitted concurrently from both transducers every 30 s. The transducers were installed at the height of 0.2 m above the channel bed using stands.

Table 3.1. Summary of the FATS experiment period.

Date of FATS experiment	Deployment site	Method of discharge estimation
9-29 June 2017	Eastern branch	Index-velocity method as described by Kawanisi et al. [35]
8-20 June 2017	Western branch	Index-velocity method as described by Kawanisi et al. [35]
6-29 November 2017	Northern branch	Two-crossing transmission lines as described by Kawanisi et al. [34] and Bahreinimotlagh et al. [43]

Similarly, the continuous monitoring of tidal discharge at the northern branch was conducted from 6 – 29 November 2017 to obtain additional data related to the phase difference

investigation at the junction. In this case, two pairs of FATS with two-crossing transmission lines configuration was used to estimate tidal discharge as proposed by Kawanisi et al. [34] and Bahreinimotlagh et al. [43]. This method is applied to show the significant variation that occurs during field investigations. The branch site of deployment transducers of FATS for two transmission lines can be seen in Figure 3.1.

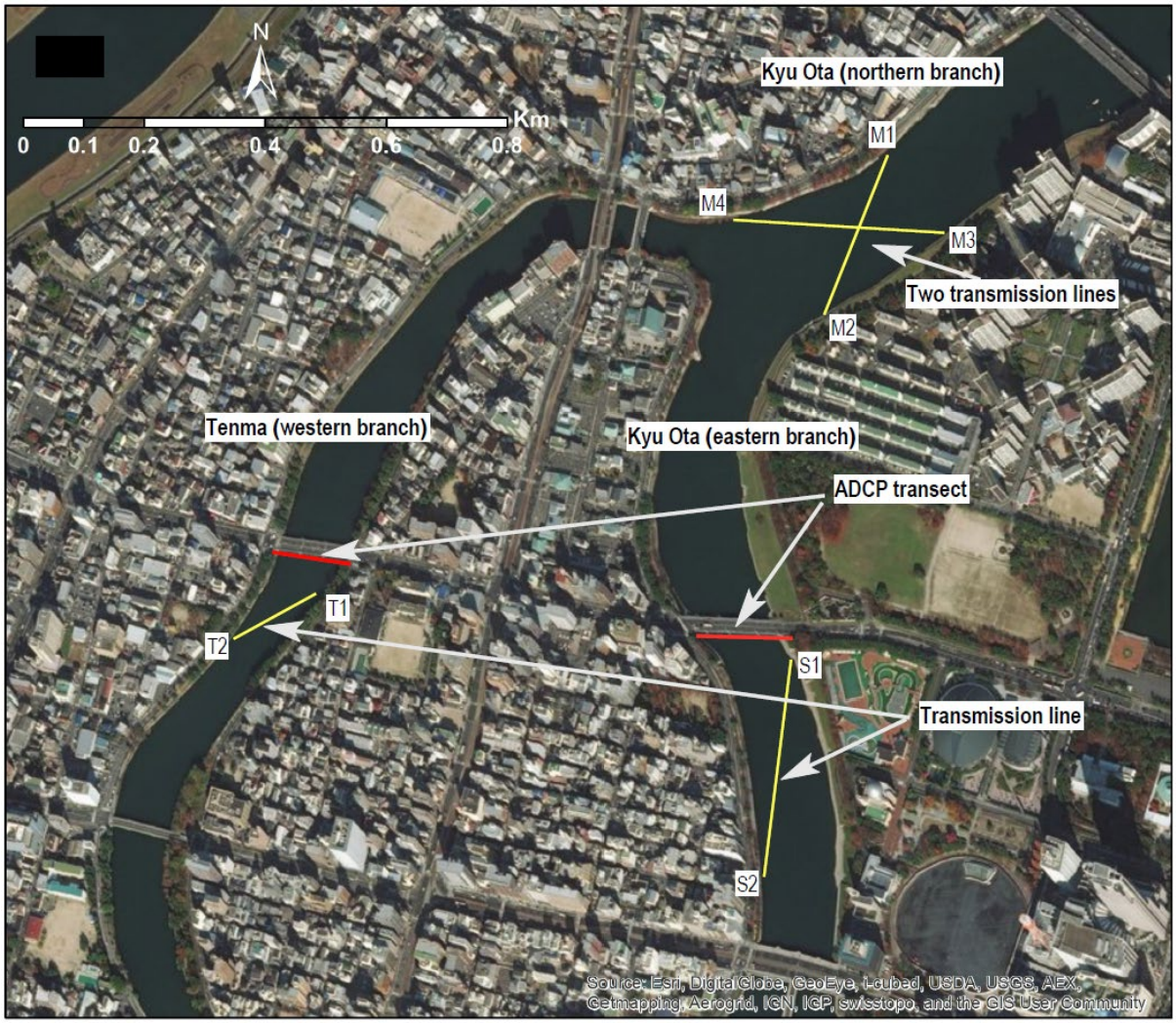

Figure 3.1. Observation site and deployment of FATS at the eastern, western, and northern branches. The yellow lines represent the transmission lines between the two transducers of FATS. S1–S2, T1–T2, and M1–M4 denote the locations of the transducers for FATS measurements. Hobo devices are attached at M1, M2, T2 and S2. The red lines denote the ADCP transects for the comparison with FATS.

In order to measure the coordinate of transducers, the author uses RTK-GPS which is capable of measuring the coordinate accurately. The accuracy of RTK GPS up to 1 cm + 1 ppm. The coordinates of the transducers and the distance between transducers for the western, eastern, and northern branches are presented in Table 3.2.

Table 3.2. Coordinates of transducers

Code	River branch	Transducers	Latitude (°)	Longitude (°)	The distance between transducers (m)
Eastern branch	Kyu Ota river	S_1	34°24′00.60	132°27′08.64	246.363
		S_2	34°23′52.68	132°27′07.32	
Western branch	Tenma river	T_1	34°24′03.80	132°26′43.63	158.836
		T_2	34°24′01.09	132°26′38.34	
Northern branch	Kyu Ota river	M_1	34°24′20.36	132°27′18.00	289.744
		M_2	34°24′20.09	132°27′06.66	
		M_3	34°24′23.49	132°27′14.52	224.639
		M_4	34°24′16.68	132°27′11.38	

3.3. Index-velocity method

Application of the index velocity method for calculating continuous records of discharge has become increasingly common, particularly since the development of acoustic-based instruments such as acoustic velocity meters (AVM) and horizontal acoustic Doppler current profilers (H-ADCP) and acoustic tomography system [35,47–49]. In this study, the index velocity method (IVM) is used to estimate the discharge based on the regression equation obtained from the relationship between the velocity parameter of ADCP measurement and velocity along the transmission line of FATS measurement as described in the previous work of Kawanisi et al. [35]. Then, the discharge can be performed as a product of the regression equation and cross-sectional area, which is a function of water depth.

3.4. ADCP campaign, cross-sectional area, and comparison with the FATS

In this study, Teledyne RDI StreamPro ADCP was used to provide and establish reference discharge data for validating FATS measurements between two seaward branches. Each ADCP campaign was conducted approximately every 5–10 min to collect the data at the bridge near the transducers (see 3.1). However, for the validation of FATS measurement in the northern branch, the ADCP campaign was carried out along the transmission line between two transducers. StreamPro ADCP was set to operate in water mode 12 with a bin size of 12 cm, the number of bin sizes set to 30, with 6 pings per ensemble. In this experiment, ADCP discharges can be obtained using WinRiver II software, in which each of the bad bin ensemble parts did not exceed 2%, while bad ensembles did not exceed 3% in each transect.

To acquire the cross-sectional area (*Ao*) as a function of water level, water level data from three branches were collected every 10 min using water level loggers (Hobo U20-001-01-Ti, Onset Co.) that were attached to the transducer stands. To obtain water level estimates, the measured pressure values should be normalized with respect to atmospheric pressure, as recorded by the barometer deployed on the riverbank. The accuracy of the water level sensors and the barometer was ±5 and ±3 mm H_2O, respectively. The post-processing of the water pressure and barometric data as parameter inputs to the software program Hoboware Pro [18].

The cross-sectional area along the transmission lines between two transducers was established by measuring the time series of the water level and bed level along the transmission line (Kawanisi et al., 2018). In order to compare and verify the discharge obtained by FATS, the moving boat ADCP was carried out to measure discharge along the transmission line between two transducers of FATS.

3.5. Bathymetry survey at channel junction

3.5.1. Bathymetry survey

The bathymetric survey of the three branches was conducted by using an autonomous boat equipped with global positioning system (GPS) device (resolution 1/10000 s) and a single beam echo sounder at a frequency of 200 kHz (resolution: 0.01 m). Transect lines were identified according to the site accessibility conditions that were assessed in the field inspection. Thus, in the case of our monitoring program, the author performed bathymetry transects for 53 sections, as depicted in Figure 3.2a. The directions of these lines are perpendicular to the stream direction, with the distance of each line being approximately 50 m (i.e., the distance between the left and right banks ≈50 m). Each transected line represents two points with the North–East coordinates based on the Japanese datum standard system. Output data of bathymetry transects obtained by the boat were stored as x, y, and z positions, where x and y represent the horizontal positions obtained from GPS recording, and z was the water depth measured by the echo sounder. The survey started at the upstream junction and finished at the downstream junction of both branches.

3.5.2. Bathymetry at the channel junction

Figure 3.2a shows the bathymetry in three branches at a tidal junction where the bed level varies between -1.5 to -4.5 T.P. m, but mostly dominated by -3 T.P. m and -2 T.P. m for the eastern and western branches, respectively. From Figures 3.2a and 3.2b, it is revealed that the eastern branch is deeper and wider than the western branch. Moreover, sedimentation was found in the western branch around 800 m from the transect 1. Similarly, the bathymetry in the northern branch shows that the width of the northern branch is wider compared to those of the eastern and the western branches. Moreover, the bed level of the northern branch is relatively constant from -2.5 T.P. m to -3.0 T.P. m.

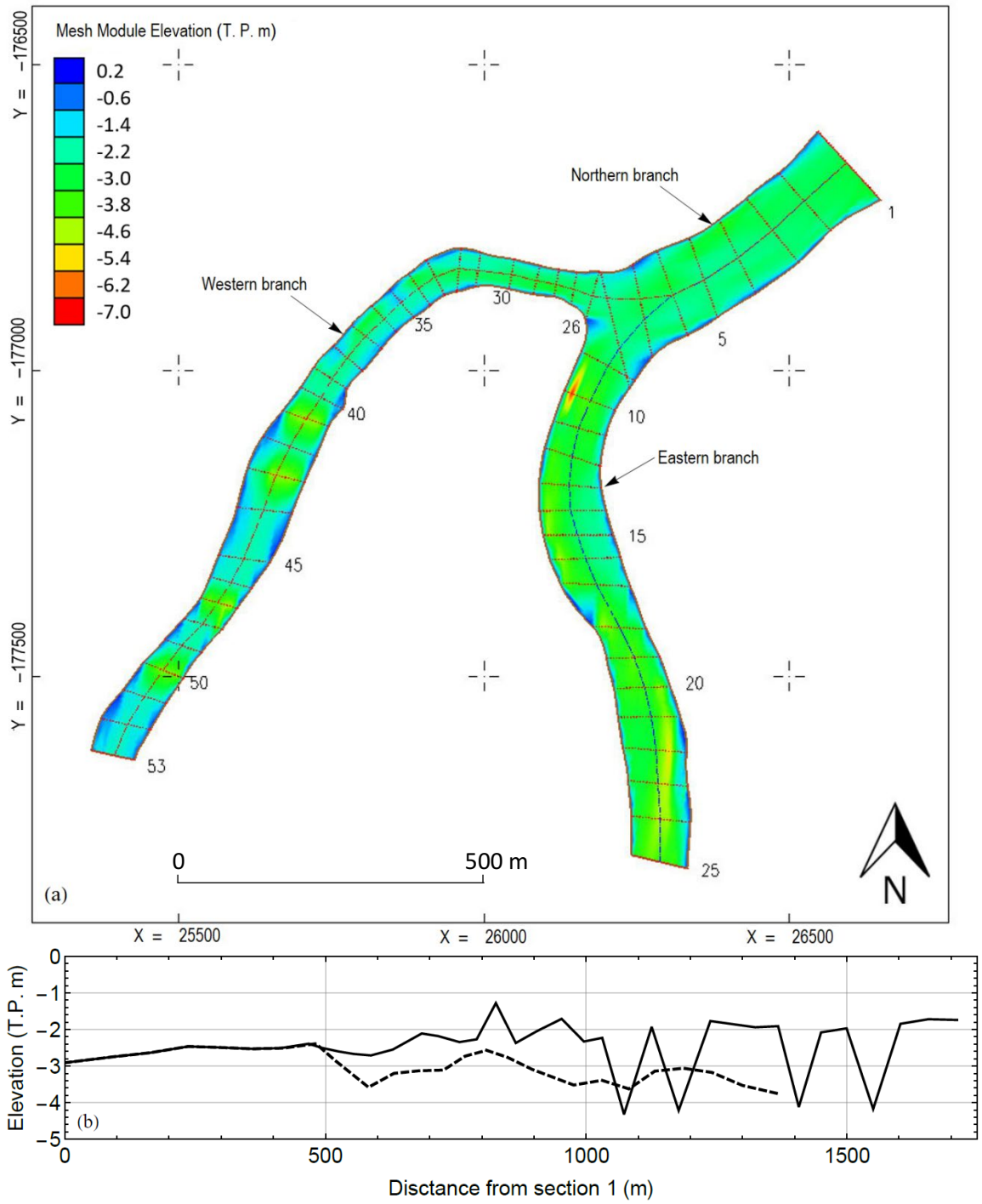

Figure 3.2. (a) Bathymetry map around the bifurcation. Elevation is measured as a vertical distance (T.P. m). The listed numbers in the range of 1–53 denote the transects of the cross-sectional line measured by the Coden boat RC–S3. (b) The longitudinal distributions of mean bed level. The black line and the black dashed lines represent the mean bed levels from the northern to the western and eastern branches, respectively.

3.6. Application of index velocity method and two-crossing transmission lines to estimating tidal discharge

3.6.1. Establishing an index velocity rating for calculating discharge

The author calculated tidal discharge by regressing the FATS index velocity with the velocity of ADCP, yielding discharge after multiplying it with the oblique cross-sectional area (A_0) along the transmission line, which varies in time as a function of water depth. Figures 3.3a and 3.3b show the linear regression relationships between the velocity of ADCP (Q_{ADCP} / A_0) and the FATS velocity along the transmission line (u_{m}) for the eastern and western branches, respectively. Both regressions show high correlation with the R^2 ~0.99.

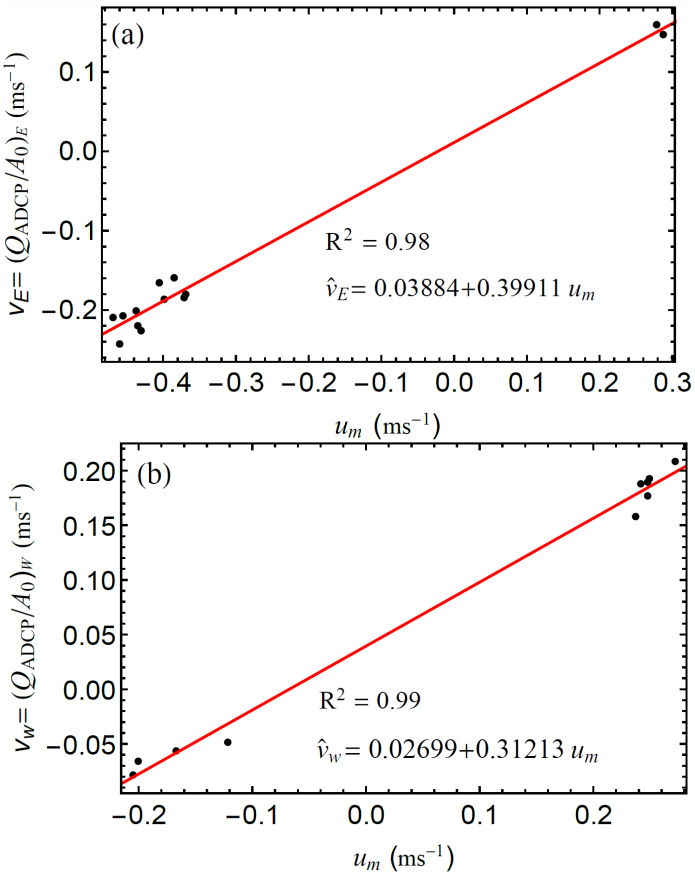

Figure 3.3. Index velocity relations for (a) the eastern and (b) western branches.

The index velocity equation used for the calculation of the cross-sectional average velocity at eastern branch ($\hat{v}_E$) and the western branch ($\hat{v}_W$) are as follows:

$$\hat{v}_E = 0.03884 + 0.39911\ u_m \quad (3.1)$$

$$\hat{v}_W = 0.02699 + 0.31213\ u_m \quad (3.2)$$

Thus, the discharge of FATS for the western and eastern branches can be respectively computed as:

$$Q_E = \hat{v}_E \times A_0 \quad (3.3)$$

$$Q_W = \hat{v}_W \times A_0 \quad (3.4)$$

3.6.2. Estimating of flow direction using two-crossed paths of FATS for calculating discharge

To determine the flow direction, the author calculate the angle (φ) between two cross transmission lines using equation 2.8 as mentioned in chapter 2, where the angle (φ) is 63.9º. Subsequently, the angle θ_1 between the transmission line S_1-S_2 and streamflow direction can be calculated by using equation 2.10 as mentioned in section 2.2.3, presented in figure 3.4a. In addition, Figure 3.4b shows the large scale of two tidal cycles of θ_1 in order to be clearly seen about the fluctuation of flow angle during the flood and ebb tide.

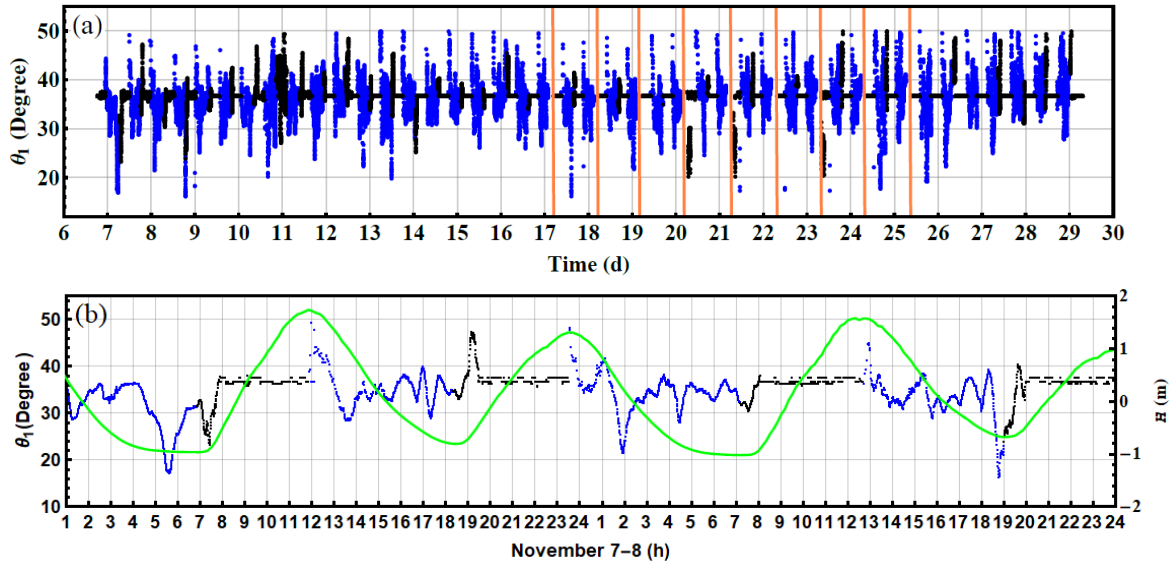

Figure 3.4. The temporal variation of flow angle measured by FATS: (a) θ_1, (b) The large scale of θ_1 during two tidal cycles on November 7-8. The vertical orange lines denote missing period. Discontinuations of the flow angle time series correspond to the missing period, as

the result of the transducers were not covered by water during the low tide. The black and blue lines denote the data during the flood and ebb tide, respectively. The green lines denote the water level (*H*).

Flow angle estimated by FATS can be converted to the flow direction in order to be verified by ADCP measurement. The results of flow direction measured from the FATS and the ADCP are plotted in Figure 3.5. The efficacy of the two crossing paths for estimating the flow direction can be seen in Table 3.3 for θ_1 where the relative difference mostly less than 10%. The mean and standard deviation of the flow direction difference ($\Delta\theta$) for θ_1 are 15.8° and -5.4°, respectively.

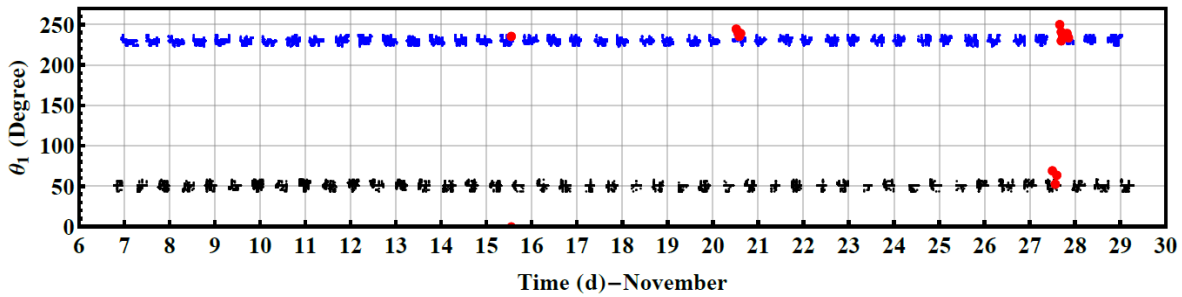

Figure 3.5. Comparison of flow direction from FATS and ADCP of θ_1

Table 3.3. Comparison of flow direction (θ_1) measured by FATS and ADCP

Date	Local time	θ_1 (°)	θ_{ADCP} (°)	$\Delta\theta = \theta_1 - \theta_{\mathrm{ADCP}}$ (°)	$\Delta\theta/\theta_{\mathrm{ADCP}}$ (%)
15-Nov-17	12:46:48	228.66	236.17	-7.51	-3.18
15-Nov-17	13:22:43	230.24	234.97	-4.73	-2.01
20-Nov-17	12:15:03	233.29	243.91	-10.62	-4.35
20-Nov-17	13:14:28	230.10	241.5	-11.40	-4.72
20-Nov-17	14:06:36	231.70	236.07	-4.37	-1.85
27-Nov-17	11:37:19	53.30	68.89	-15.59	-22.63
27-Nov-17	13:13:52	51.49	52.80	-1.32	-2.49
27-Nov-17	14:34:03	51.72	64.13	-12.41	-19.35
27-Nov-17	16:09:35	230.40	250.46	-20.06	-8.01
27-Nov-17	16:57:07	232.91	241.14	-8.23	-3.41
27-Nov-17	17:35:10	226.55	234.96	-8.41	-3.58
27-Nov-17	18:20:39	234.55	235.06	-0.51	-0.22
27-Nov-17	19:49:15	227.26	238.64	-11.38	-4.77
27-Nov-17	20:24:41	229.18	234.17	-4.99	-2.13

To illustrate the flow direction comparison obtained by FATS and ADCP, the author compare it in the map. In addition, the numerical model results (see chapter 5) are also be used to evaluate the flow direction obtained by FATS and ADCP in the northern branch.

The results in Figure 3.6, Figure 3.7 and Figure 3.8 show that FATS result is nearly equal with the model and seems more realistic compared to the ADCP results, qualitatively. For instances, the flow direction during flood tide between FATS and ADCP results are similar with the model (See Figure 3.6). Furthermore, the flow direction during the ebb tide between FATS and ADCP results are little different, but FATS result with the model seems the same (See Figure 3.8).

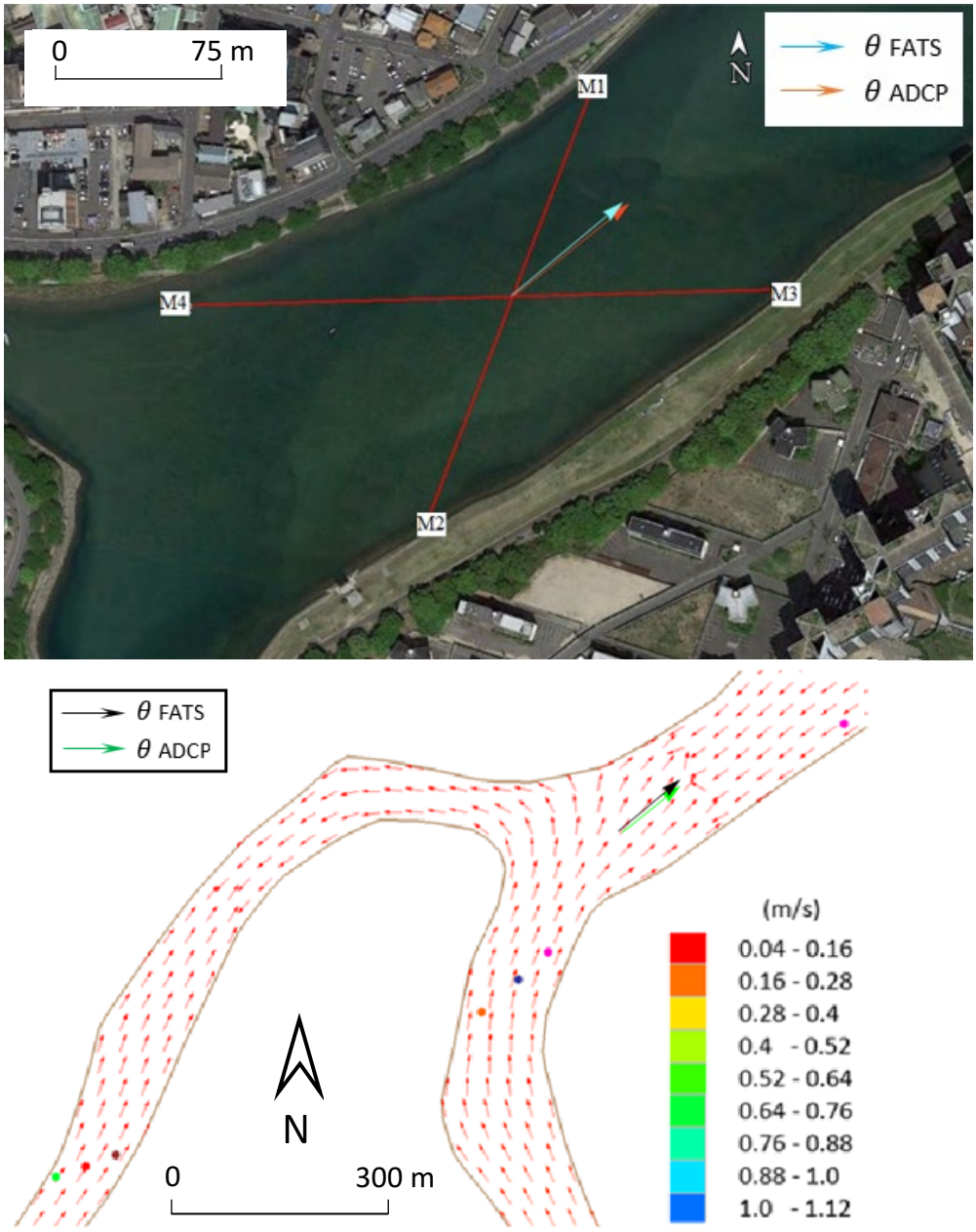

Figure 3.6. Plotting flow directions for the case θ_{FATS}= 51.49 ° and θ_{ADCP} =52.80 ° (top) between FATS and ADCP, (bottom) between FATS, ADCP and Model. The red arrows in the model are the flow velocities vector.

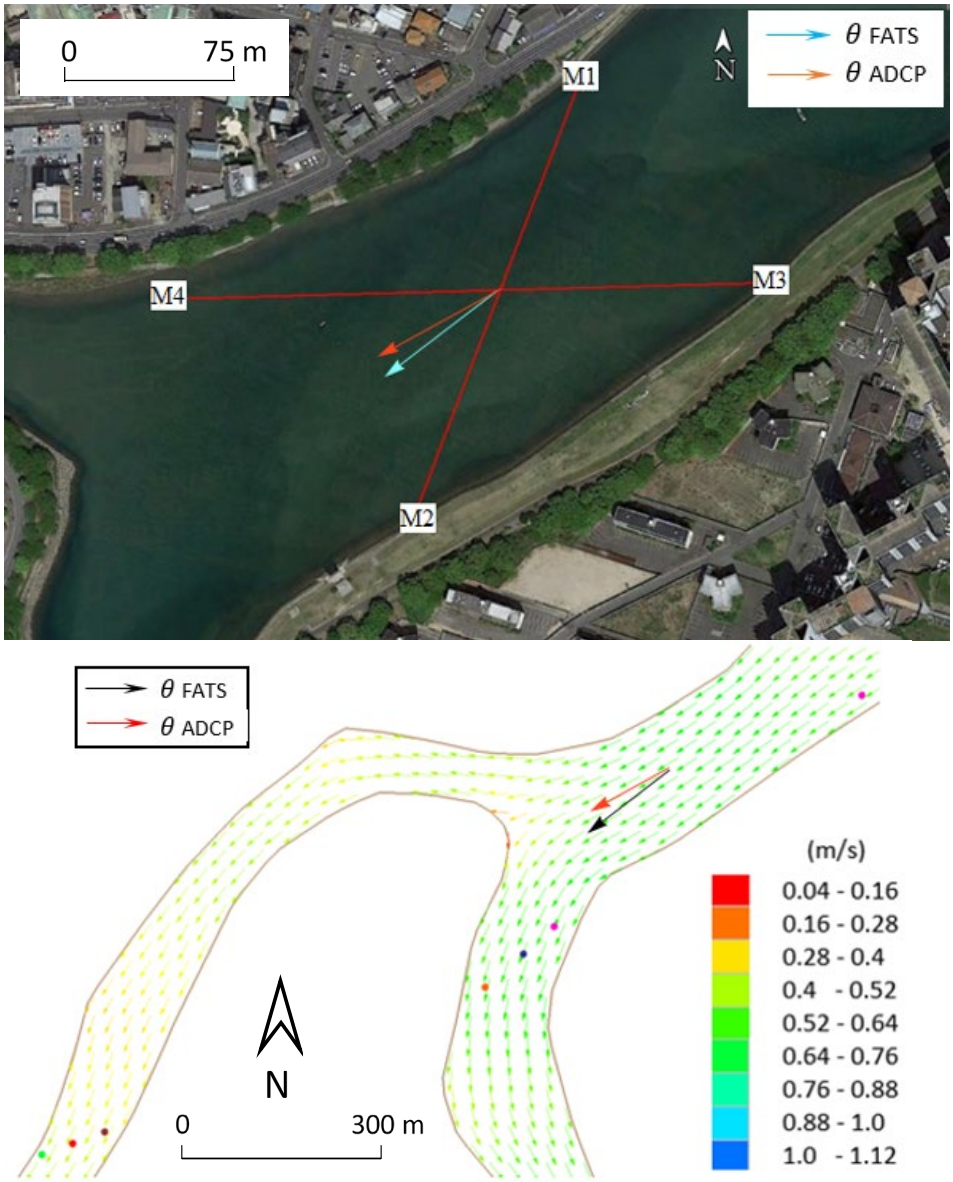

Figure 3.7. Plotting flow directions for the case θ_{FATS} = 232.91 ° and θ_{ADCP} =241.14 ° (top) between FATS and ADCP, (bottom) between FATS, ADCP and Model. The green and yellow arrows in the model are the flow velocities vector.

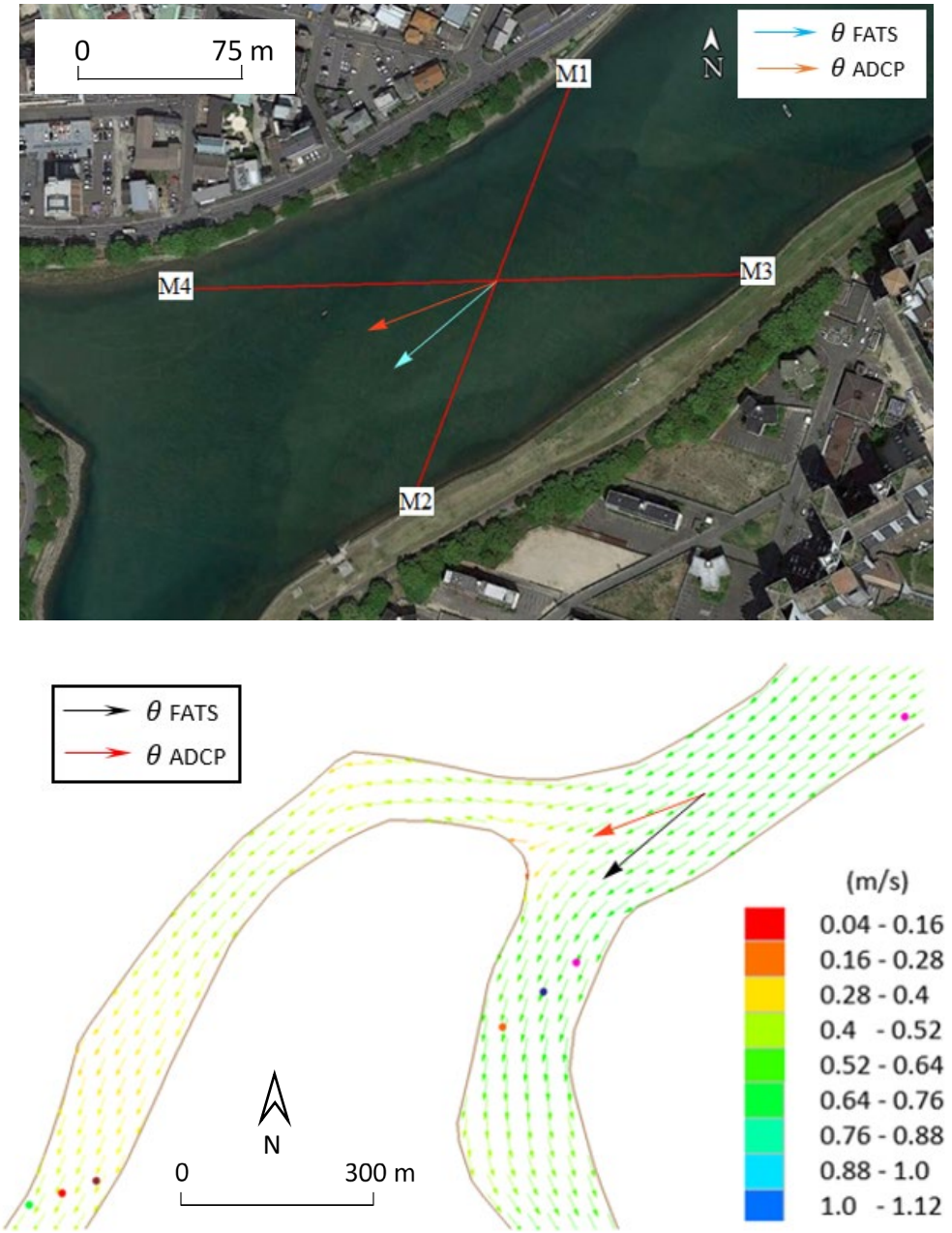

Figure 3.8. Plotting flow directions for the case θ_{FATS}= 230.40 ° and θ_{ADCP} =250.46 ° (top) between FATS and ADCP, (bottom) between FATS, ADCP and Model. The green and yellow arrows in the model are the flow velocities vector.

3.7. Validation of discharge measurement obtained by FATS

The FATS results were validated by the moving-boat ADCP measurements as shown in Figure 3.9a, 3.9b, and 3.9c for the eastern, western, and northern branches, respectively. It is

important to note that in the eastern branch, the validation using ADCP measurement is limited due to ship traffic.

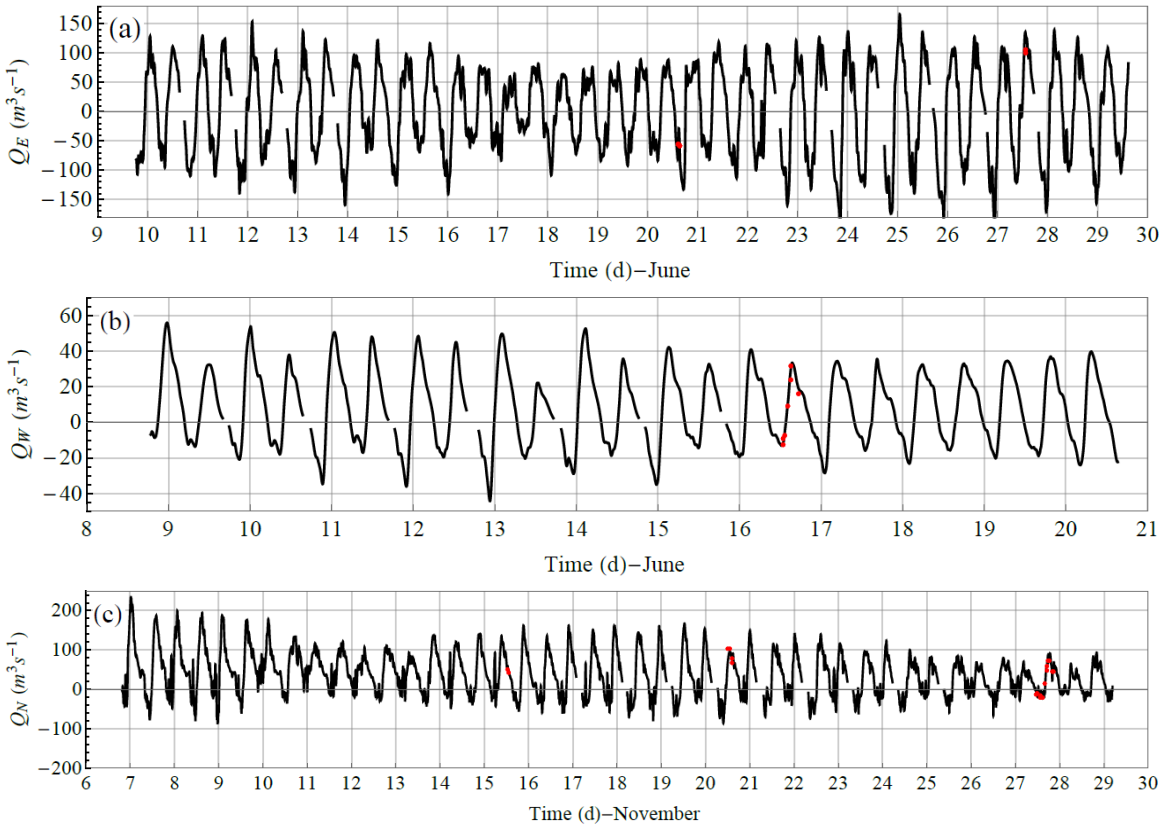

Figure 3.9. Temporal variations of : (a) tidal discharge at the eastern branch, (b) tidal discharge at the western branch, and (c) tidal discharge at the northern branch. The red dots denote the discharge obtained using moving-boat ADCP measurements. Discontinuations of the discharge time series correspond to the missing period, as the result of the transducers were not covered by water during low tide.

The differences between ADCP and FATS probably due to several reasons: i) tidal flow was inhomogeneous which causes a complex stream field [50], ii) fluctuations in the stream direction can potentially induce errors in FATS measurement [34].

The relative difference of discharges estimated from ADCP measurements and FATS are mostly ranged from ~0.4% to ~10% as shown in Table 3.4, Table 3.5, and Table 3.6. The results are consistent with those of previous works where the relative differences between

FATS and ADCP estimates are ranges from 1% to 10% [35,42,43]. Moreover, the author can evaluate how closely the FATS estimates match ADCP results using the equation of root mean square error (RMSE):

$$\text{RMSE} = \sqrt{\frac{\sum_{i=1}^{n}[Q_{\text{FATS}}(t_i) - Q_{\text{ADCP}}(t_i)]^2}{n}} \tag{3.5}$$

where $Q_{\text{ADCP}}(t_i)$ and $Q_{\text{FATS}}(t_i)$ correspond to the observed and calculated discharge at time t_i, respectively; and n is the number of data points. Thus, based on the data obtained from Table 3.4, Table 3.5, and Table 3.6, the root means square error (RMSE) at the eastern branch is 5.0 m^3s^{-1} or only ~1.67 % of the discharge range, whereas the RMSE of the western branch is 1.68 m^3s^{-1} or ~1.7 % of the discharge range. Similarly, the root mean square error of FATS at the northern branch is 5.3 m^3s^{-1} or ~1.65 % of the discharge range. Thus, FATS measurement results are reliable estimates of the discharge in a tidal estuary.

Table 3.4. Comparison between FATS and ADCP measurements at the eastern branch

Date	Local time	Q_{FATS} (m^3s^{-1})	Q_{ADCP} (m^3s^{-1})	$\Delta Q = Q_{\text{FATS}} - Q_{\text{ADCP}}$ (m^3s^{-1})	$\Delta Q/Q_{\text{ADCP}}$ (%)
June 20, 2017	14:44:05	-57.56	-55.67	-1.89	3.40
June 20, 2017	14:55:13	-58.53	-55.67	-2.86	5.14
June 20, 2017	15:07:31	-59.09	-58.81	-0.28	0.48
June 20, 2017	15:16:31	-60.31	-58.41	-1.90	3.25
June 20, 2017	15:27:11	-65.81	-58.18	-7.63	13.11
June 27, 2017	13:29:25	108.38	99.55	8.83	8.87
June 27, 2017	13:41:38	109.60	104.65	4.95	4.73

Table 3.5. Comparison between FATS and ADCP measurements at the western branch

Date	Local time	Q_{FATS} (m^3s^{-1})	Q_{ADCP} (m^3s^{-1})	$\Delta Q = Q_{\mathrm{FATS}} - Q_{\mathrm{ADCP}}$ (m^3s^{-1})	$\Delta Q/Q_{\mathrm{ADCP}}$ (%)
June 16, 2017	12:45:11	-11.75	-12.2	0.45	-3.69
June 16, 2017	12:59:19	-10.26	-9.13	-1.13	12.38
June 16, 2017	13:09:38	-8.05	-7.37	-0.68	9.23
June 16, 2017	13:14:28	9.80	8.91	0.89	9.99
June 16, 2017	14:14:28	25.19	24.26	0.93	3.83
June 16, 2017	14:53:59	31.85	31.47	0.38	1.21
June 16, 2017	15:13:13	31.17	27.17	4.00	14.72

Table 3.6. Comparison between FATS and ADCP measurements at the northern branch

Date	Local time	Q_{FATS} (m^3s^{-1})	Q_{ADCP} (m^3s^{-1})	$\Delta Q = Q_{\mathrm{FATS}} - Q_{\mathrm{ADCP}}$ (m^3s^{-1})	$\Delta Q/Q_{\mathrm{ADCP}}$ (%)
November 15, 2017	12:46:48	52.98	49.68	3.3	6.64
November 15, 2017	13:22:43	43.67	42.95	0.72	1.68
November 20, 2017	12:15:03	88.61	103.34	-14.73	-14.25
November 20, 2017	13:14:28	95.68	104.48	-8.80	-8.42
November 20, 2017	14:06:36	78.95	78.64	0.31	0.39
November 27, 2017	11:37:19	-10.07	-10.75	0.68	-6.33
November 27, 2017	13:13:52	-17.80	-19.41	1.61	-8.29
November 27, 2017	14:34:03	-18.16	-20.15	1.99	-9.88
November 27, 2017	16:09:35	14.32	15.24	-0.92	-6.04
November 27, 2017	16:57:07	57.83	57.73	0.10	0.17
November 27, 2017	17:35:10	73.36	73.61	-0.25	-0.34
November 27, 2017	18:20:39	77.10	71.55	5.55	7.76
November 27, 2017	19:49:15	41.15	45.65	-4.50	-9.86
November 27, 2017	20:24:41	48.85	44.98	3.87	8.60

3.8. Error analysis of discharge measurement obtained by FATS

3.8.1. Error analysis of discharge measurement obtained by FATS for index velocity method

The relative error affecting the discharge measurements estimated by FATS can be evaluated to quantify the contributions of each term to the total error. The total error structure of FATS measurements is presented below

$$\left|\frac{\delta Q}{Q}\right| = \left|\frac{\delta H_m}{h_m}\right| + \left|\frac{\delta z_{Bm}}{h_m}\right| + \left|\frac{\delta u_m}{u_m}\right| + \left|\frac{\delta\theta}{\cos\theta \sin\theta}\right| \quad (3.6)$$

where H_m is the mean water level, z_{Bm} is the mean elevation of the river bed along the transmission line measured by moving-boat ADCP, u_m is the cross-sectional average velocity along the transmission lines, and θ is the flow angle between the transmission line and streamflow direction. The first $\left|\frac{\delta H_m}{h_m}\right|$ and second terms $\left|\frac{\delta z_{Bm}}{h_m}\right|$ are related to the inadequate measurements of water level and water depth, while the bathymetry of the river was measured using moving-boat ADCP. The maximum error of FATS measurement will occur at minimum water depth (under the shallow water condition). The third term $\left|\frac{\delta u_m}{u_m}\right|$ is the error that arises owing to the velocity resolution of FATS measurements. The velocity resolution (u_r) of FATS measurements is one of the significant sources of errors, particularly during the low-flow conditions [42]. It can be expressed as,

$$u_r = \frac{c_m^2}{2L}\frac{1}{2f} \quad (3.7)$$

where c_m is sound speed (≈ 1450-1500 ms^{-1}), f is the central frequency of the transducer (30 kHz), and L is the distance between two transducers. The last term $\left|\frac{\delta\theta}{\cos\theta \sin\theta}\right|$ corresponds to the flow angle error.

The error increased at decreasing water depths (h_m). The minimum water depth during the experiment is h_m = 0.6 m. For $|\delta H_m|$= 0.01 m, $\left|\delta z_{B_m}\right|$= 0.01 m, the first and second term

error contribute $\left|\frac{\delta H_m}{h_m}\right|$ =1.25% and $\left|\frac{\delta z_{B_m}}{h_m}\right|$ = 1.25%, respectively. The velocity resolution (u_m) can be increased using equation (3.7), as a result, $|\delta u_m|$ for S1-S2 (eastern branch) and T1-T2 (western branch) are 0.0159 ms^{-1} and 0.0139 ms^{-1}, respectively. Thus, the third terms $\left|\frac{\delta u_m}{u_m}\right|$for S1-S2 and T1-T2 account for 3.2 – 3.9 % and 4.6 – 6.9 %, respectively. The fourth term $\left|\frac{\delta\theta}{\cos\theta \sin\theta}\right|$ corresponds to the flow angle error of streamflow. The last term is approximately 4.6 % for eastern branch with θ_{eastern} = 25º, and 6% for western branch with θ_{western} = 18º, and $\delta\theta$ = 1º. Thus, the total error for the S1-S2 and T1-T2 are within the ranges of 9.7 – 10.4 % and 13.1 – 15.4 %, respectively. This result seems to be consistent with the previous results of Kawanisi et al. [35] and Bahreinimotlagh et al. [43] where the relative errors are within 8-14% and 19%, respectively.

3.8.2. Error analysis of discharge measurement obtained by FATS for two crossing transmission lines

The relative errors affecting the discharge measurements measured by FATS can also be evaluated using equation 3.6. The error increased at decreasing water depths (h_m). The minimum water depth during the experiment is h_m = 0.6 m. For $|\delta H_m|$= 0.01 m, $\left|\delta z_{B_m}\right|$= 0.01 m, the first and second term error contribute $\left|\frac{\delta H_m}{h_m}\right|$ =1.25% and $\left|\frac{\delta z_{B_m}}{h_m}\right|$ = 1.25%, respectively. The velocity resolution (u_m) can be increased using equation (3.7), as a result, $|\delta u_m|$ for M1-M2 and M3-M4 are 0.0135 ms^{-1} and 0.0184 ms^{-1}, respectively. Thus, the third terms $\left|\frac{\delta u_m}{u_m}\right|$for M1-M2 and M3-M4 account for 2.3 – 4.6% and 1.5 – 2.7%, respectively. The fourth term $\left|\frac{\delta\theta}{\cos\theta \sin\theta}\right|$ corresponds to the flow angle error of streamflow. Smaller flow angles will induce larger errors. Therefore, with $\delta\theta$ = 2.3 – 4.3º, the last term supplies the relative error of the M1-M2 transmission line (8.4 – 15.7 %) and M3-M4 transmission line (9.8–18.4 %). Thus, the

total error for the M1-M2 and M3-M4 are within the ranges of 13.2 – 22.8 % and 13.8 – 23.6 %, respectively. This result seems to be consistent with the previous works of Kawanisi et al. [35] and Bahreinimotlagh et al. [43] where the relative errors are within 8-14% and 19%, consecutively.

3.9. Time series of the tidal discharge in the western, eastern, and northern branches

Figure 3.10a shows the temporal variations of the water levels and discharges in the eastern and western branches, whereas 3.10b shows the temporal variations of the water levels and discharges in the northern branches. The time series of water level and tidal discharge in three branches show the semidiurnal characteristic, i.e., the high tide and low tide occur two times a day. Additionally, a fortnightly change in the tidal discharge amplitude is discovered wherein the tidal discharge is larger during the spring tide than that of during the neap tide.

The temporal variation of discharges in the branches show different behavior where the eastern and western branches range from -157 to 155 m^3s^{-1} and -42 to 58 m^3s^{-1}, respectively. From the comparison of the tidal discharges between the eastern and western branches as shown in Figure 3.10a, it is revealed the tidal discharge of the eastern branch is approximately 2–6 times greater than that of the western branch during flood and ebb tides. This is caused by the difference in the geometry of both branches, i.e., the water depth and the channel width of eastern branch are much larger than that of the western branch as can be seen in Figure 3.2.

Furthermore, the profile of tidal discharge at the western branch is also much more asymmetric compared to that of the eastern branch where the discharge during the ebb tide was higher than during the flood tide. Similarly, Figure 3.10b shows the temporal variation of water level and tidal discharge at the northern branch located at the upstream junction where the tidal discharge ranged from -90 to 230 m^3s^{-1}.

Figure 3.10c shows the temporal variation of the water level and tidal velocity for the eastern and western branches, whereas Figure 3.10d describes the tidal velocity and water level at the northern branch. The temporal variation of tidal velocity at the eastern, western, and northern branches range from -0.28 to 0.3 ms^{-1}., -0.12 to 0.19 ms^{-1}, and -0.5 to 1 ms^{-1}, respectively.

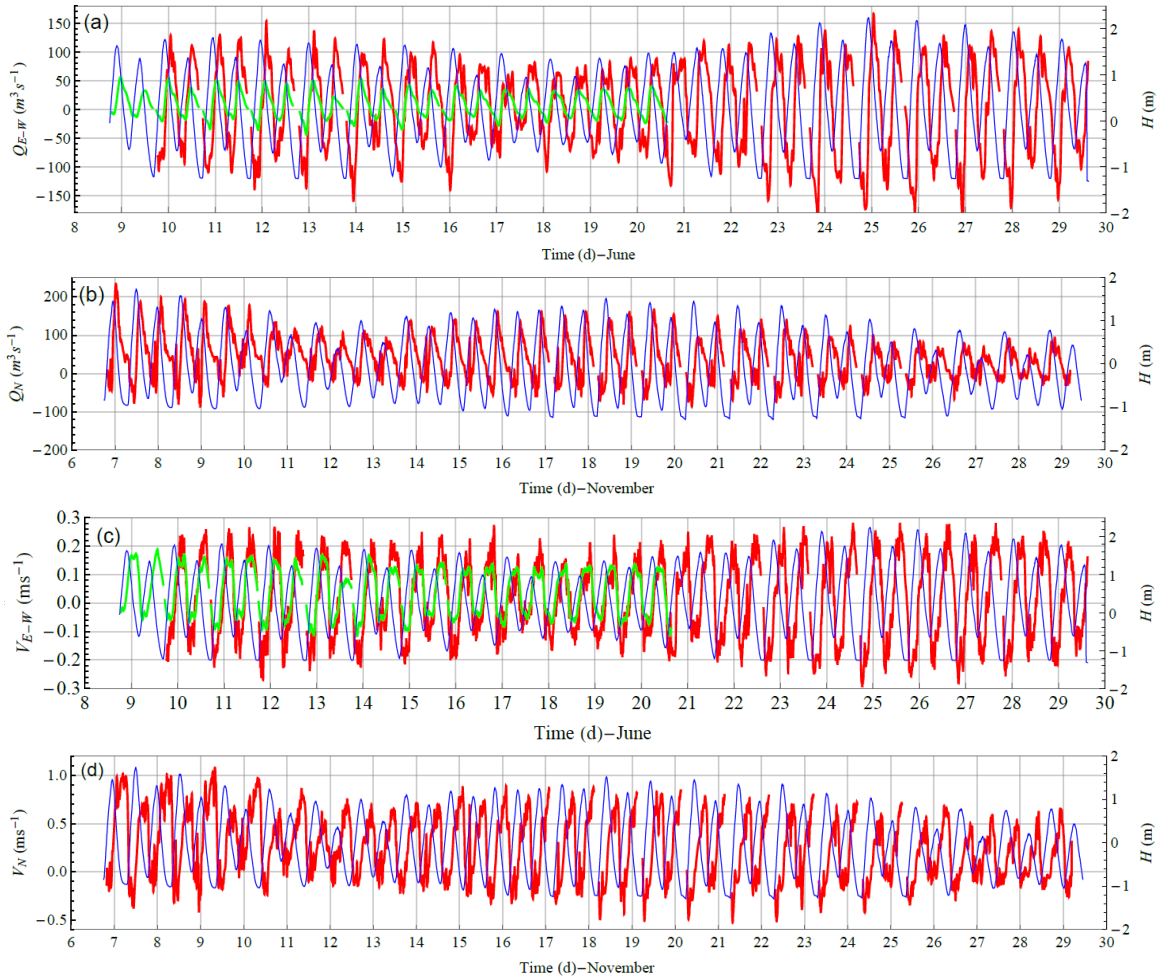

Figure 3.10. Temporal variations of (a) water level at the eastern branch (blue line), tidal discharge at the eastern branch (red line), and tidal discharge at the western branch (green line). (b) Water level at the northern branch (blue line) and tidal discharge at the northern branch (red line). (c) Water level at the eastern branch (blue line), tidal velocity at the eastern branch (red line), and tidal velocity at the western branch (green line). (d) Water level at the northern branch (blue line) and tidal velocity at the northern branch (red line). Positive discharge and velocity coincide with the seaward flow.

3.10. Subtidal discharge division in the western and eastern branches

The purpose of quantifying subtidal discharge division is to explore the temporal variation of flow division and the inequality of streamflow during the spring and neap tide. In this study, the author uses the subtidal discharge obtained by applying a Battle–Lemarie filter of wavelet function. The division of subtidal tidal discharge between the eastern and western branches at a tidal junction can be quantified using the discharge asymmetry index (ψ), as proposed by Buschman et al. [1].

$$\psi = \frac{\langle Q_E \rangle - \langle Q_W \rangle}{\langle Q_E \rangle + \langle Q_W \rangle} \tag{3.8}$$

The tidal discharge asymmetry index (ψ) is zero for an equal discharge division, ψ = 1 when all river water flows through the eastern branch, and ψ = -1 when the western branch carries all the discharge. Therefore, a positive value is obtained when the discharge at the eastern branch is greater than that at the western branch and vice versa.

Due to the difference in lengths of the data obtained from the FATS measurements between the eastern and western branches, only data from June 10–20, 2017 were used to calculate the discharge asymmetry index (ψ) using equation 3.8.

Figure 3.11 shows the discharge asymmetry index and subtidal discharge variation in the eastern and western branches from 10 to 21 June, suggesting that the temporal variations in subtidal discharge of the eastern branch are slightly larger than those of the western branch, except within 18 and 19 June, the variation was almost the same during the neap tide.

Moreover, Figure 3.11 shows the temporal variation in the discharge asymmetry index during spring and neap tide. The discharge asymmetry index fluctuates in the range of −0.02 to 0.26 from 10 to 21 June, showing the inequality of flow division between the eastern and western branches, where the eastern branch can distribute larger discharge than that in the

western branch during spring tide; the flow division between the western and eastern branch is nearly equal during the neap tide (18 to 19 June).

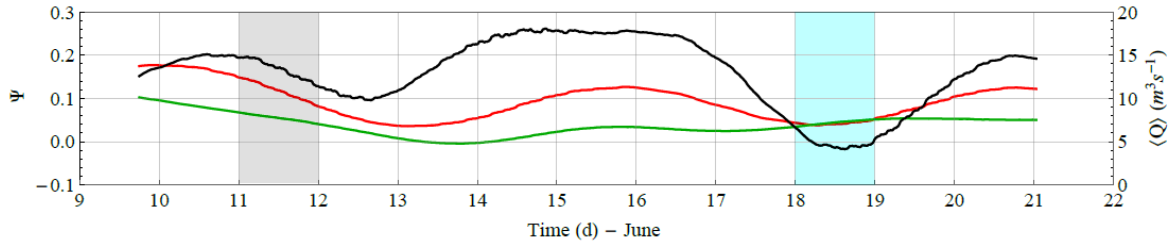

Figure 3.11. Discharge asymmetry index (black line). Temporal variations of subtidal discharges in the eastern (red line) and western branch (green line)**.** The grey and blue highlighted boxes represent the spring and neap tide, respectively.

3.11. Interpretation of flow division in two seaward branches

Based on the bathymetry map as presented in Figure 3.2, the depth and width of the eastern branch are greater than those of the western branch. However, the inequality of flow division at the tidal junction cannot be calculated using only a ratio of the wetted cross-sectional areas between the two branches [2], because the hydrodynamic process at the tidal junction is also strongly influenced by the spring and neap tide, as well as by the asymmetrical geometry shape between the two seaward branches.

The response of tidal dynamic to the local geometry between two seaward branches displays different characteristics, where the asymmetric discharge at the western branch is more prominent compared to the eastern branch [51]. The asymmetric tidal discharge observed at the western branch indicates that the ebb discharge is larger than the flood discharge. On the contrary, the characteristic of tidal discharge at the eastern branch is nearly equal during the ebb and flood tide. As shown in Figure 3.2, the western branch is shallower and narrower than the eastern branch. Therefore, the propagating tidal wave in shallow and narrow branches, and modulated with the river discharge, can generate the nonlinear effect as a result of interaction with the local topography [9,28]. This nonlinear effect leads to the generation and development

of shallow-water constituents, which cause tidal distortion and asymmetry [28]. This asymmetric tidal discharge can induce a seaward sediment movement [29].

Regarding the flow division characteristic at the tidal junction of Ota River, our findings are depicted in Figure 3.11. The discharge asymmetry index ranges from −0.02 to 0.26 during the 10 to 21 June, suggesting that the eastern branch has the capability to deliver greater amounts of subtidal discharge, approximately 55%–63% compared with the western branch. However, the flow division is nearly equal during the neap tide (i.e., from 18 to 19 June) [51].

Figure 3.11 shows that the equality of asymmetry index between the eastern and western channels can be observed clearly during the neap tide period. Nevertheless, the inequality of flow division is obviously prominent during the spring tide duration. This phenomenon can happen because the fluctuation in the subtidal discharge at the eastern branch is greater than that at the western branch; the subtidal discharge at the eastern branch decreases during the neap tide, so that both subtidal discharges are nearly equal during the neap tide [51].

3.12. Conclusions

To investigate the flow division of subtidal discharge between the two seaward branches (eastern and western branches), the discharge asymmetry index was used. Moreover, to characterize the tidal discharge behavior and its relationship with the water level and modulated with the freshwater discharge, the phase difference is investigated.

The response of tidal dynamic to the local geometry between two seaward branches shows that the asymmetric discharge at the western branch is more pronounced compared with the eastern branch. The asymmetric tidal discharge at the western branch indicates the ebb discharge is larger than the flood discharge. This can happen because the interaction between tidal propagation and the local geometry of western branch that modulated by river discharge could generate the nonlinear effect. This nonlinear effect leads to generation and development

of shallow-water constituents, which cause tidal distortion and asymmetry. This asymmetric tidal discharge can induce a seaward sediment movement. In contrast, the characteristic of tidal discharge at the eastern branch is nearly equal during the ebb and flood tide.

Regarding the flow division characteristic at the tidal junction of Ota River, the temporal variation of subtidal discharge in the western branch is relatively constant without relation with the tidal range, while in the eastern branch the temporal variation of subtidal discharge is relatively varied.

The discharge asymmetry index varies from −0.02 to 0.26 during the studied period, suggesting that the eastern branch has the capability to deliver greater amounts of subtidal discharge, approximately 55%–63% compared with the western branch, except during the neap tide where the flow division is nearly equal between the eastern and western branches. This can happen because the temporal change in the flow division is induced by the fluctuation in the subtidal discharge at the eastern branch. The subtidal discharge decreases during the neap tide, so that both subtidal discharges are nearly equal.

Chapter 4. The phase difference between the tidal discharge and water level at a tidal channel junction

4.1. Introduction and purpose

The phase difference between the tidal discharge and water level in the estuary receives little attention from researchers, particularly at the channel junction of estuaries. Horrevoets et al. [4] investigated the phase difference along the single channel of the estuary and suggested that the river discharge can control the phase difference. They pointed out that the phase difference in the downstream area is mostly constant, whereas in the upstream part of estuary the phase difference is not constant. Additionally, the phase difference can become negative in the upstream area. Savenije et al. [52] stated that the phase difference is a basic and significant parameter to describe the characteristic of tidal wave propagation in an estuary. It is strongly affected by estuary shape and is also a function of the ratio between bank convergence and tidal wavelength.

Nevertheless, based on the previous works mentioned above, the temporal variation of phase difference at a tidal channel junction is still unidentified. The change of phase difference in an estuarine system can identify the hydrodynamic processes such as amplification and damping of tidal wave [5,6]. Besides, when the phase difference is near quadrature (close to $\sim 90°$), the duration asymmetry of water level can induce asymmetries in tidal current magnitude in the estuary channel [7]. More importantly, the phase difference can even influence subtidal transport of flow, sediment, and saltwater in the estuarine system [8,9].

The aim of this chapter is to identify the phase difference in tidal discharge in the channels that are connected to the junction. To further explore the phase difference at a junction, two unidentified issues have been taken into account: (i) the temporal variation of the phase difference in each branch connected to the junction, and the dominant factors that influences

the phase difference between the two seaward branches; (ii) the influence of spring-neap tide on the phase difference.

4.2. Wavelet method for tidal wave analysis

A non-stationary signals are frequently encountered in a variety of engineering fields (e.g. wind, ocean, and earthquake engineering). To analyze nonstationary time series signal, wavelet method is used instead of Fast Fourier transform (FFT). FFT method has the capability to analyze the frequency of time series data (frequency domain) and power/energy, but does not provide the information in the time domain, when the frequency occurs [25]. Moreover, the FFT has the disadvantage to analyze the nonstationary data because the FFT has only a single set of basis functions that includes only sine and cosine function. Although FFT based method called the short-term Fourier transform (STFT) can provide time and frequency localization through a narrow window, but the high resolution cannot be achieved in both time and frequency domains simultaneously. This happened because the window must be chosen for locating sharp peaks or low frequency features, as a result of the inverse relation between window length and the corresponding frequency bandwidth [53]. In contrast, the wavelet method can analyze the nonstationary data of time series in the domain time, frequency, and power [54] because of having an infinite set of possible basis functions [55]. Worldwide, engineer uses it for many purposes in various area, such as geophysical, hydrology, and oceanography [53].

Currently, wavelet transformation is an advanced analysis method in signal processing particularly used in investigating hydrodynamic processes in an estuary such as tidal wave and their interaction with the river discharge [7,8,25]. Wavelet method was also favored compared to traditional harmonic analysis due to its ability to deal with non-stationary signals. More specifically, wavelet method can also be applied to investigate the phase difference between the time series of water level and velocity in estuary. Thus, the wavelet is a power tool to

analyze the tidal flow and the phase difference between the tidal discharge and water level in a multi-channel estuary.

The continuous wavelet transformation (CWT) is to apply a wavelet transformation to a time series of tidal signals. The CWT is determined using scaled and the normalized wavelets is defined as a convolution of time series signal *H(t)* as follows [25]:

$$W_k^X(s) = \sqrt{\frac{\delta t}{s}} \sum_{k'=1}^{M} H_{k'}\, \psi_0 \left[\left(k' - k \right) \frac{\delta t}{s} \right] \tag{4.1}$$

where s is the time scale ; k and k' are time series; δt is the uniform time step (10 minutes in this study) and M is the length of the time series; ψ_o is a normalized wavelet function to have unit energy at each scale. The Morlet wavelet is a function used in CWT for tidal analysis [25]. The Morlet wavelet function is as follows.

$$\psi(\gamma) = \pi^{-1/4} e^{i\omega_0 \gamma} e^{-0.5\gamma^2} \tag{4.2}$$

where ω_0 is dimensionless frequency and γ is dimensionless time. In this analysis, ω_0 is set to 6 for tidal analysis because it provides a good balance between time and frequency resolution [56]. The cross-wavelet transformation (XWT) of two time series x_k and y_k can be defined as $W^{XY} = W^X W^{Y*}$, where * represents complex conjugation [56].

In this section, three functions of wavelet analysis are used to investigate the time-series signal between tidal discharge and water level, that is, continuous wavelet transformation (CWT), cross-wavelet transformation (XWT), and wavelet coherence (WTC). CWT is used to detect variations in time series and their simultaneous representation in the time–frequency space, and also to determine the dominant period. Moreover, CWT analysis can display temporal and spatial evolutions of tidal frequency spectra [19]. XWT was utilized to analyze the phase difference between the two-time series. The phase difference is basically the phase

angle represented by the arrow, that is, the arrow pointing right means both signals travel in the same direction (in-phase), the arrow pointing left means both signals travel in the opposite direction (anti-phase), and the arrow pointing down means the first time series of signal leads the second one by 90°. WTC is used to find significant coherence between the two-time series and to show the confidence level, and is given as

$$R_k^2(s) = \frac{\left|O\left(s^{-1}W_k^{XY}(s)\right)\right|^2}{O(s^{-1}|W_k^X(s)|^2).O(s^{-1}|W_k^Y(s)|^2)} \tag{4.3}$$

where *O* is a smoothing operator. In this study, the authors uses the open software developed by Grinsted. Details of the wavelet are referred to Grinsted et al. [56].

The accuracy of wavelet analysis result is based on two parameters [57], i.e., the strong relationship (coherence) between two time series of data, and the cone of influence (COI) which represents the edge effects in the beginning and ending of the time series, corresponding to 1.5 days on each end. As a result, the minimum length of time series data for analyzing using wavelet method approximately more than 3 days.

4.3. The phase difference between the water level and tidal discharge

Tidal discharge (Q) varies along the channel in estuaries and co-varies with the tidal wave. One of the most important parameters in estuary processes is a phase difference between the water level and the tidal discharge [13]. There are two methods to determine the type of wave in estuarine channels, that is, phase lag and phase difference [12,25]. The phase lag is the time lag between high water slack (HWS, i.e., when the discharge is zero) and high water (HW, i.e., when the water level is maximum) [6,12]. In contrast, the phase difference is the time lag between the peak tidal discharge and the HW [12,25]. Therefore, there is a relationship between the phase difference and the phase lag, that is, $\varepsilon + \varphi = \frac{\pi}{2}$, where ε is the phase lag and φ is the phase difference [6,26]. In this study, the author uses the phase difference to describe the

relation between the tidal discharge and water level [25,27]. If φ= 90° is a standing wave, φ= 0° is propagating, and 0° < φ< 90° is a mixed wave. The illustration of phase difference Δφ between standing wave, progressive wave and mixed wave can be seen in Figure 4.1a,4.1b, and 4.1c, respectively.

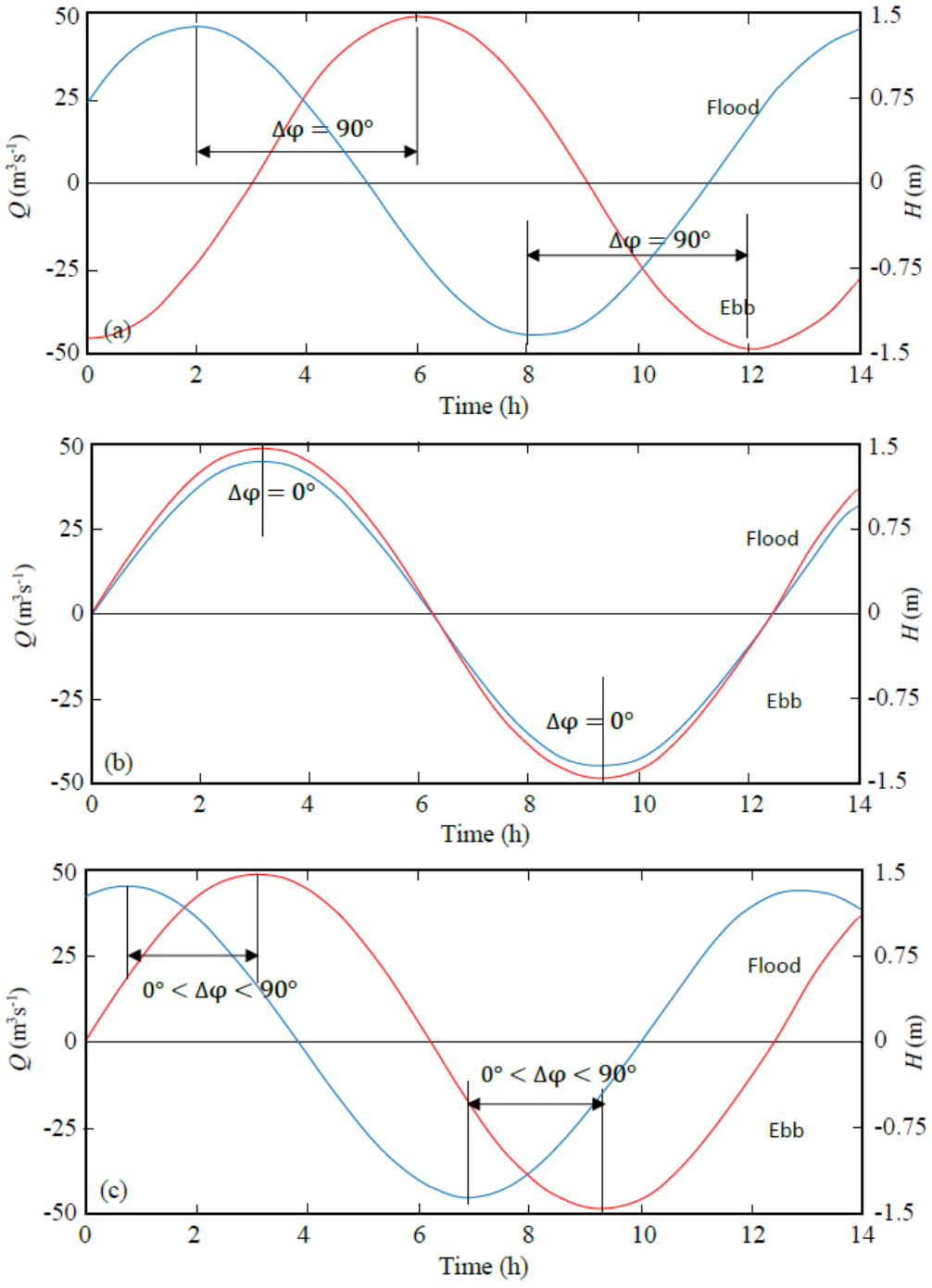

Figure 4.1. (a) Standing wave (b) progressive wave (c) mixed wave. The red and blue line represent water level and tidal discharge, respectively.

The standing wave is mostly a characteristic for a short estuary with a length equal to the $\lambda/4$, where λ in this case is the wave length of tide. In addition, a standing wave can occur in such a semi-enclosed bay. In a special case, a standing wave can also happen if such a closing structure blocks the wave propagation (a reflected wave). On the other hand, a progressive wave only occurs in a frictionless channel of constant cross-sectional area (deep water channel of constant cross-sectional area). A mixed wave usually occurs in alluvial estuary. Alluvial estuary is defined as estuary in which the bed and banks are made up of a variety of materials such as silt, clay, sand and gravel [58]. In addition, the channels in alluvial estuary have a variety of morphological pattern such as straight, meandering, and braided channel [59].

4.4. The wavelet method for analyzing the interaction between the tidal discharge and water level in the three branches

Figures 4.2 shows three figures consisting of CWT, XWT, and WTC analyses between the tidal discharge and water level at the eastern branches. From the figures, the dark red color background denotes a strong power spectrum, suggesting a dominant tidal signal. The vertical bar shows the energy of the tidal domain. From the CWT and WTC analyses, the semidiurnal signal is more dominant than the diurnal signal. Moreover, the semidiurnal domain is always present during the spring and neap tide, whereas the diurnal domain is only present during spring tide, but fades during the neap tide. Thus, the tide of the Ota River is characterized by the mixed-semidiurnal tide. Besides the semidiurnal and diurnal signal, the author can also identify the quarter-diurnal in the eastern branch, which is discontinuous and weak. In contrast, the fortnightly signal cannot be detected. From XWT analysis, the phase difference between the tidal discharge and the water level at the eastern branch can be denoted by the black arrows pointing straight down at ~78°.

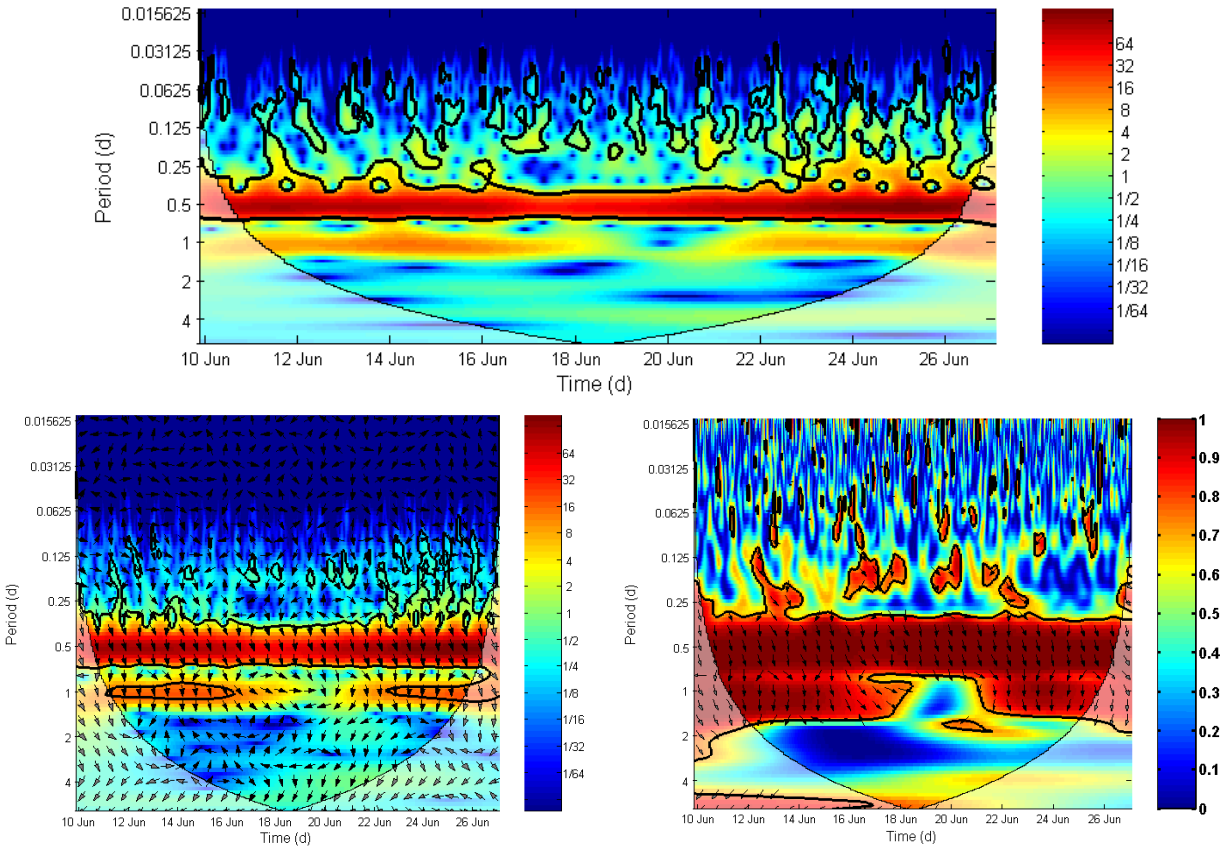

Figure 4.2. Wavelet analyses in eastern branch: (top) continuous wavelet transformation; (bottom left) cross-wavelet transform; (bottom right) wavelet coherence. The black contours represent the 0.95 confidence level against red noise, and the cone of influence (COI) where edge effects might distort the picture is shown as a lighter shade. The wavelet power is $\log_2(A^2/v)$, where A is the wavelet amplitude and v is the variance of the original tidal signals. The y-axis in the CWT and XWT is on a $\log_2$ scale.

Similarly, Figure 4.3 shows three plots consisting of CWT, XWT and WTC analyses between the tidal discharge and water level in the western branches. The semidiurnal domain is always present, whereas the diurnal domain is only present during spring tide but diminishes during the neap tide. The author can recognize the quarter-diurnal in the western branch which is discontinuous and weak, but more pronounced compared to the eastern branch. The fortnightly signal is also cannot be identified in the western branch. From XWT analysis, the phase difference between the tidal discharge and the water level at the western branch shows that the black arrows are pointing down at ~88.5°.

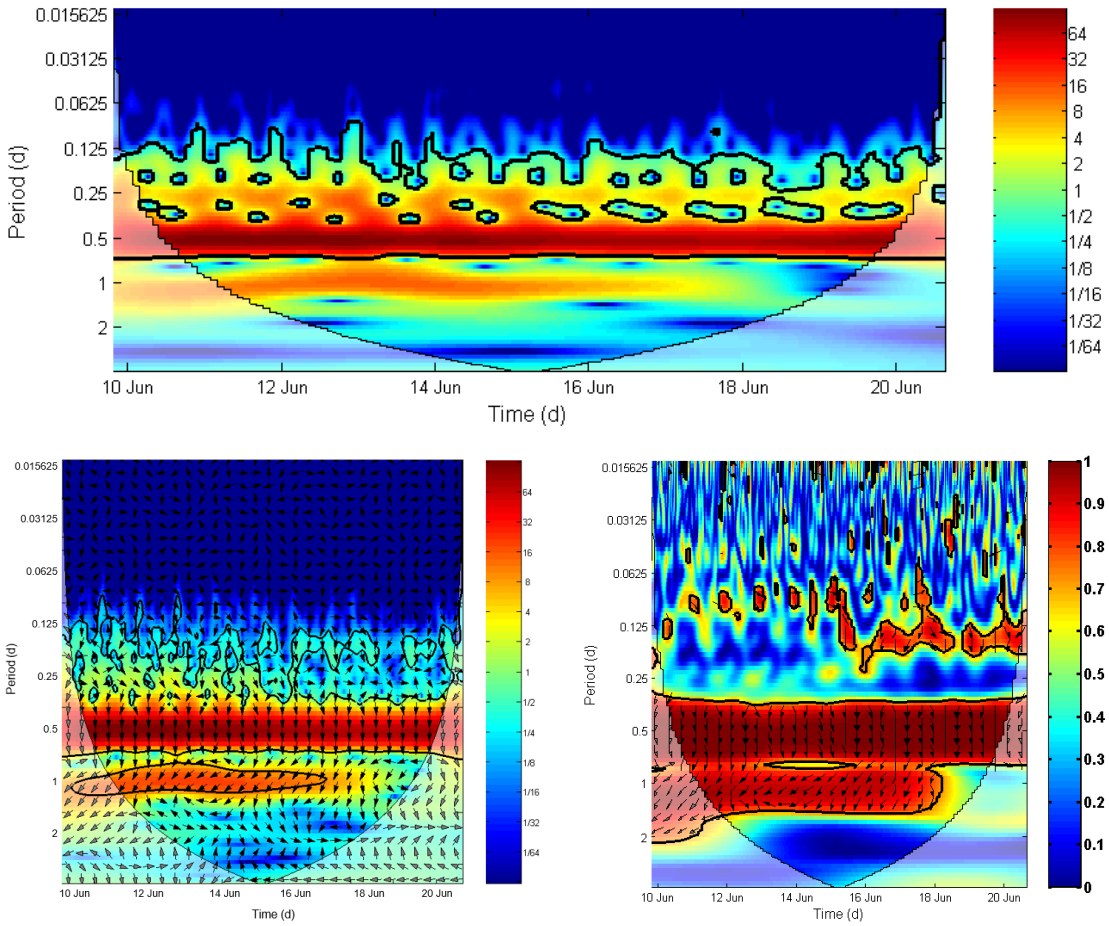

Figure 4.3. Wavelet analyses in western branch: (top) continuous wavelet transform. (bottom left) cross-wavelet transform. (bottom right) wavelet coherence. The black contours represent the 0.95 confidence level against red noise and the cone of influence (COI) where edge effects might distort the picture is shown as a lighter shade. The wavelet power is $\log_2(A^2/v)$, where A is the wavelet amplitude, v is the variance of the original tidal signals. The y-axis in the continuous wavelet transformation (CWT) and cross-wavelet transformation (XWT) is on a $\log_2$ scale.

The phase difference in tidal discharge between the western and eastern branches was further examined to ensure that the tidal discharge phase of the eastern branch is greater than that of the western branch. Figure 4.4 confirms that the tidal discharge phase at the western branch is larger than the discharge phase at the eastern branch, with a phase difference of ~11°. Moreover, it also seems that the geometry of the branch has a greater effect on the behavior of the phase difference at the western branch compared with the eastern branch.

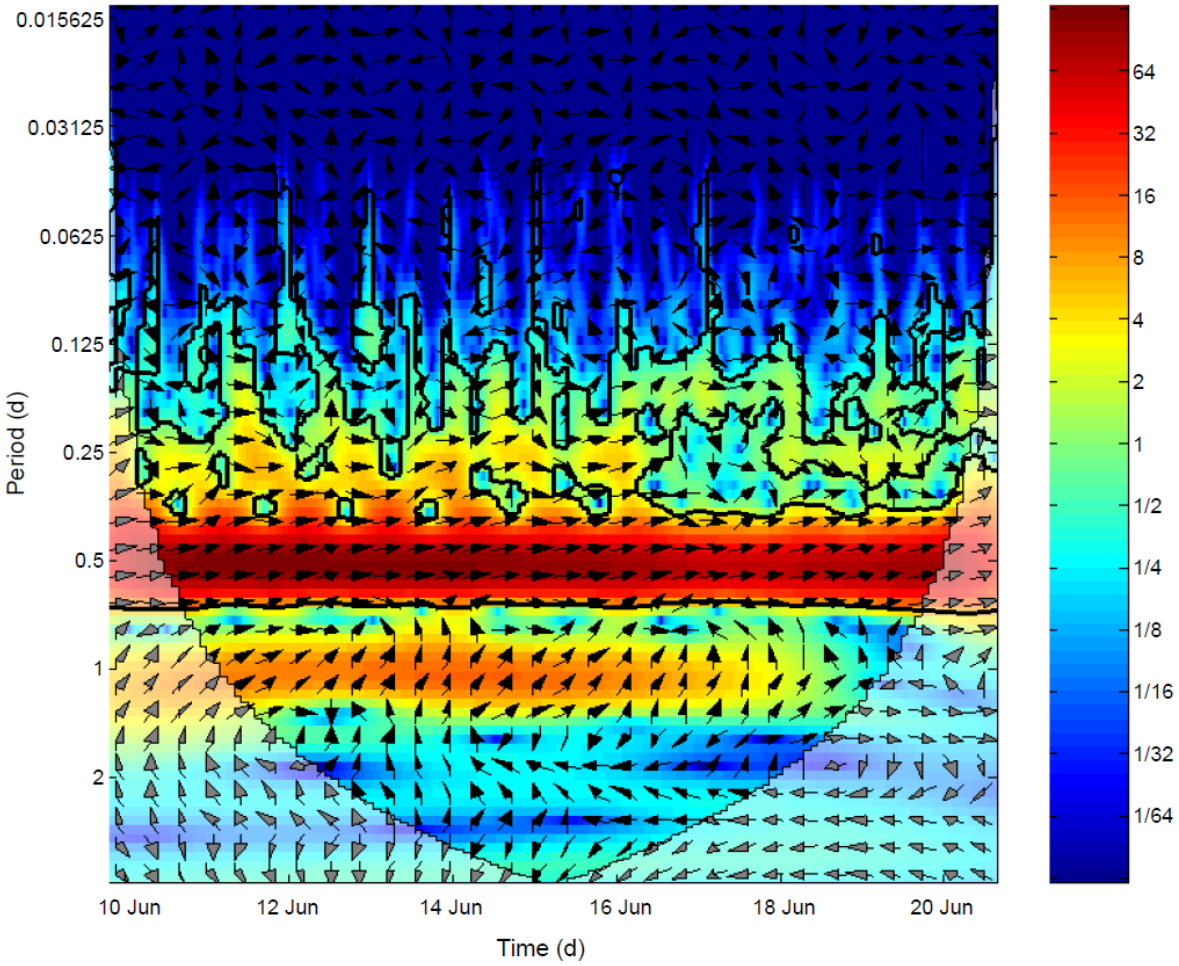

Figure 4.4. The phase difference in the tidal discharge phase between the eastern and western branches. The black contours represent the 95% confidence level for red noise, and the cone of influence (COI) where edge effects might distort the picture is shown as a lighter shade. The wavelet power is $\log_2(A^2/v)$, where A is the wavelet amplitude and v is the variance of the original tidal signals. The y-axis is on a $\log_2$ scale.

As mentioned in Section 3.2, to gain a comprehensive understanding of phase difference behavior around the junction, an additional observation campaign at the northern branch using FATS is needed to collect the tidal discharge continuously. With this, the phase difference before and after the junction can be investigated completely.

Figure 4.5 shows the wavelet analysis at the northern branch, consisting of CWT, XWT, and WTC analyses between the tidal discharge and water level. The semidiurnal domain is always present, whereas the diurnal domain is only present during spring tide, but disappears during the neap tide. The author can recognize the quarter-diurnal in the northern branch, which

is discontinuous and weak, but more pronounced compared with that in the eastern branch. The fortnightly signal also cannot be detected.

The phase difference during semidiurnal is ~90°. This result confirms that the phase difference at the northern branch shows slightly increased behavior compared with the seaward branches (eastern and western branches). This result indicates that the behavior of phase difference is slightly increased after passing through the junction into the northern branch (a landward branch of the junction).

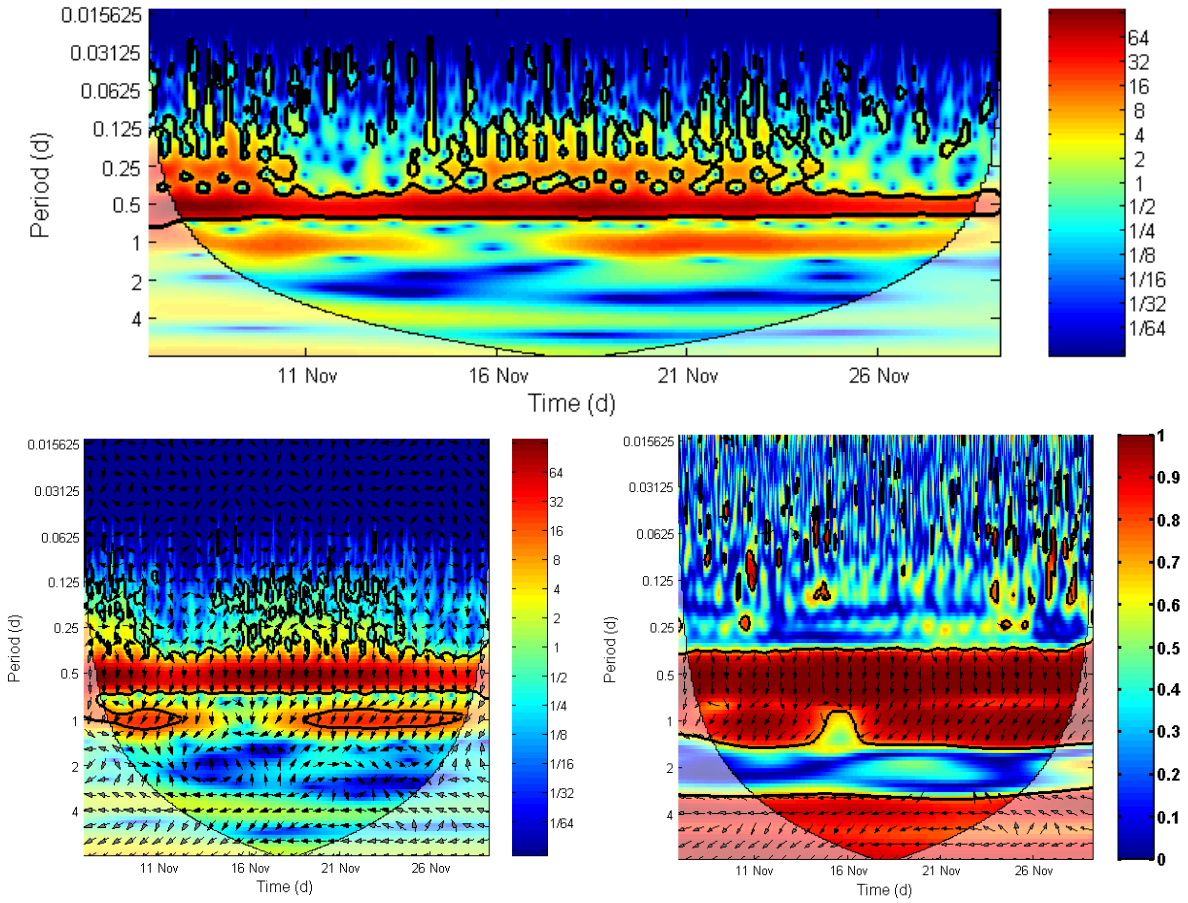

Figure 4.5. Wavelet analyses in the northern branch: (top) continuous wavelet transform; (bottom left) cross-wavelet transform; (bottom right) wavelet coherence. The black contours represent the 0.95 confidence level against red noise, and the cone of influence (COI) where edge effects might distort the picture is shown as a lighter shade. The wavelet power is $\log_2(A^2/v)$, where A is the wavelet amplitude and v is the variance of the original tidal signals. The y-axis in the CWT and XWT is on a $\log_2$ scale.

4.5. Interpretation of the phase difference in the three branches

CWT analysis recognizes the semidiurnal and diurnal signal in three branches connected to the junction. The quarter-diurnal signal can be detected, but is not dominant, because the signal energy is weak and discontinuous. This happened because the shallow water effect in the branch does not influence tidal distortion of D2, and thereby cannot produce enough energy to transform from D2 to D4 [23,28]. Moreover, the tidal junction is located in the middle of estuary, which is still near to the river mouth, implying that the tide needs to travel more in the landward direction to generate D4.

In contrast, the fortnightly tidal signal does not appear in the CWT analysis in the relationship between the tidal discharge and water level possibly because of two reasons, that is, (i) the time-series data are too short for capturing fortnightly signal; or (ii) freshwater discharge is very low. For comparison with the work of previous researchers, for example, the work of Leonardi et al. [8], the fortnightly signal does not exist in their wavelet analysis over period of 1.5 months, with the freshwater discharge ranging from 110 to 8235 m^3s^{-1}. On the contrary, Sassi et al. [3] could recognize the fortnightly tide using longer time-series data over the period of six months, with the freshwater discharge ranging from 3000 to 5000 m^3s^{-1}. However, in our case, the time-series data are less than one month, with the freshwater discharge in the Ota estuary during normal condition ranging from 20 to 40 m^3s^{-1}. Thus, in the case of the Ota River, the absence of a fortnightly signal in the interaction between the water level and tidal discharge is the result of the short time-series data [22].

Two main questions arise about the characteristic of phase difference at the junction: (i) the first regarding the variation of the phase difference between the two seaward branches (the eastern and western branches). As a follow-up question, what is the dominant factor that influences the phase difference between the two seaward branches? and (ii) is the phase difference influenced by the spring and neap tide?

To answer the first question, the author must first determine the phase difference between the two branches. The phase difference between the tidal discharge and water level at the eastern and western branches for semidiurnal are ~78° and ~88.5°, indicating a mixed wave and mimic standing wave, respectively [51]. It is important to note that the phase difference range of 78° to 88.5° implies that the tidal discharge leads the water level. The discharge phase difference between the eastern and western branches shows that the discharge phase at the western branch leads by ~15 minutes compared with the discharge phase at the eastern branch.

Figure 4.6 shows the temporal variation of phase difference between the tidal discharge and water level in the eastern and western branches. Both phase differences are relatively constant.

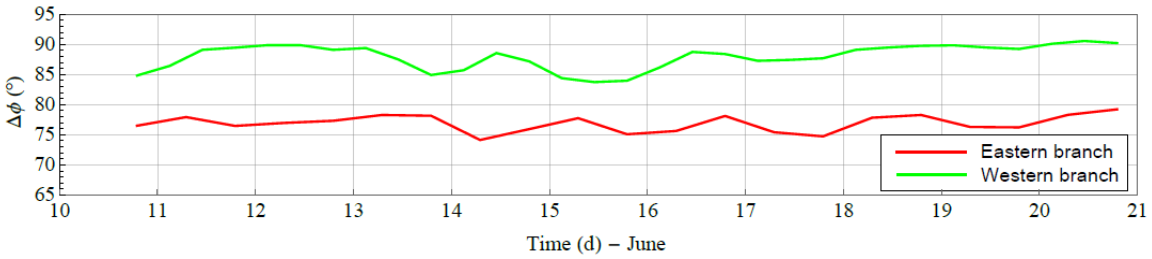

Figure 4.6. Temporal variation of phase difference between the tidal discharge and water level in the eastern and western branches

In addition, the phase difference between the tidal velocity and water level for the eastern and western branches is ~71° and ~80°, respectively (figures not shown). Thus, the phase difference between the velocity and water level is consistent with the phase difference between the discharge and water level, where the phase difference in the western branch is larger than that in the eastern branch. The author wants to investigate further the reason that the phase difference at the western branch is higher than at the eastern branch. According to Savenije [24], the phase difference is strongly affected by the convergence shape effect, rather than river discharge and bottom friction. Accordingly, the author quantify the convergence levels between the eastern and western branches using the exponential function form with three

important parameters; namely, the mean water depth, river width, and cross-sectional area, as exemplified by Savenije et al. and Cai et al. [12,31].

Figure 4.7. shows the geometry of both the eastern and western branches. The geometry analysis presented in Figure 4.7 (right) obviously indicates that the western branch is more convergent compared with the eastern branch, as shown in Figure 4.7 (left). More convergent means the upstream part of western branch is narrower or sharper compared to the eastern branch. The phase difference behaves differently in two different geometry. The narrower the channel geometry, the larger the phase difference. As a result, the phase difference in the western branch is larger than in the eastern branch [51]. This happened because the narrower channel can hamper the tidal propagation [13,24]. From the results of phase difference characteristic and the geometry analysis between two seaward branches, it can be inferred that the amplitude of tidal wave at the western branch near the junction is more magnified compared with at the eastern branch [5,11].

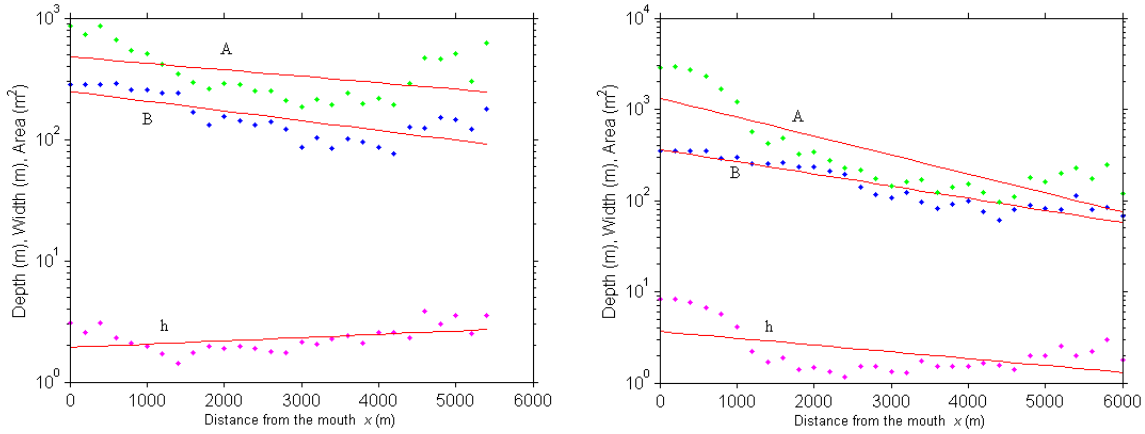

Figure 4.7. Geometry of the eastern branch (left) and western branch (right); showing the longitudinal variation of cross-sectional area (A), the width (B) and the depth (h).

Figure 4.5 shows that the phase difference between the tidal discharge and water level at the northern branch (a landward branch of the junction) is ~90°, indicating a standing wave. Thus, it is important to note that the phase difference at the northern branch is slightly higher than that of the two seaward branches. This evidence indicates that the phase difference is

slightly increased after passing through the junction into the northern branch. However, further investigation is needed to confirm this evidence [51].

The answer for the second question is that the effect of spring and neap tide on the phase difference in the semidiurnal domain is negligible. As shown in Figure 4.4, the phase difference between two seaward branches changes slightly during the spring and neap tide. The phase difference between the tidal discharge and water level is relatively constant, where during the spring tide, the phase difference is ~11°, whereas during the neap tide, the phase difference is ~9°. Also, in Figure 4.6, the phase difference in the eastern and western branch are relatively constant. Therefore, the change of the phase difference between spring and neap tide is not significant. This phenomenon is probably because the phase difference is a function of a ratio between bank convergence and tidal wave length [24]. Moreover, the phase difference can be affected by two factors, that is, the river discharge [8,24] and topography of the estuarine channel, also known as estuary shape [24].

The upstream discharge from Yaguchi gauging station during the experiment is relatively constant, ranging from 20 to 40 m^3s^{-1} during June 2017, though the freshwater discharge from Yaguchi gauging station increased slightly from 20 to 90 m^3s^{-1} in November 2017. Thus, during this condition, the tidal processes of the Ota River can be classified as a tidally dominated estuary [8]. Additionally, this finding is still more or less consistent with the work of Leonardi et al. [8], who pointed out that the phase difference always tends to be close to 90° as long as the characteristic of flow is bidirectional.

4.6. Conclusions

The wavelet analyses of the temporal variation of the phase differences between the two seaward branches show slightly different behavior. A mimic standing wave characteristic ($\Delta\varphi = \sim 88.5°$) occurs at the western branch, whereas a mixed wave characteristic ($\Delta\varphi = \sim 78°$) occurs at the eastern branch. It is shown that the phase difference between tidal discharge

and the water level is relatively constant during the neap and spring tide. The discharge phase at the western branch leads the discharge phase at the eastern branch by ~ 15 minutes. Additionally, the geometry analysis between the two seaward branches reveals that the western branch is more convergent compared with the eastern branch, and thus causes a larger phase difference compared with the eastern branch. As a result, the amplitude of tidal wave at the western branch near the junction is more magnified compared with the eastern branch.

Using the same analysis, the author can say the phase difference between the tidal discharge and water level at the northern branch (a landward branch of the junction) indicates a standing wave characteristic ($\Delta\varphi = \sim 90°$), which is slightly higher than the phase difference in the two seaward branches. This evidence implies that the phase difference is slightly increased after passing through the junction into the northern branch. Further study is needed to explore the characteristics of the phase difference in the larger area of the multi-channel estuary.

Chapter 5. Investigation of flow velocity and subtidal salinity using FATS and simulating 2D velocity distributions at a tidal channel junction using a 2D numerical model

5.1. Introduction and purpose

Investigating the dynamics of tidal velocity and salinity in a multi-channel estuary are of paramount importance for the maintenance of channels, water usage and the estuarine management [24,25,60]. The temporal variation of tidal velocity is an essential parameter in a tidal channel network to transport sediment, nutrients, and contaminant [2]. The behavior of velocity pattern along the channels mainly influenced by geometrical shape [13]. More specifically, Buschman et al. [1] emphasized that the inequality of flow division is also controlled by the tidal junction. As a result, velocity/discharge in one branch can be different from that of another branch.

In order to measure both mean velocity and salinity continuously in a tidal channel junction, an innovative fluvial acoustic tomography system (FATS) will be used. This chapter applies FATS to estimate temporal variation of velocity and salinity in a multi-channel estuary, particularly at a tidal channel junction. In addition, a numerical model is also used to analyze flow field pattern at the tidal channel junction.

This chapter consists of three works, i.e., (i) calculation of tidal velocity at the tidal channel junction using FATS during high flow (flood event) and normal flow condition, (ii) calculation of salinity at the tidal channel junction using FATS, and (iii) investigating the 2D velocity distributions at the tidal junction using RMA 2 flow model.

5.2. Methods

5.2.1. Field site

Figure 5.1. shows the experiment site of FATS deployment at the tidal channel junction in Ota River estuary. As mentioned in section 3.5.2., the eastern branch is deeper and wider than the western branch. Similarly, the topography in the northern branch shows that the width of the northern branch is wider compared to those of the eastern and the western branches.

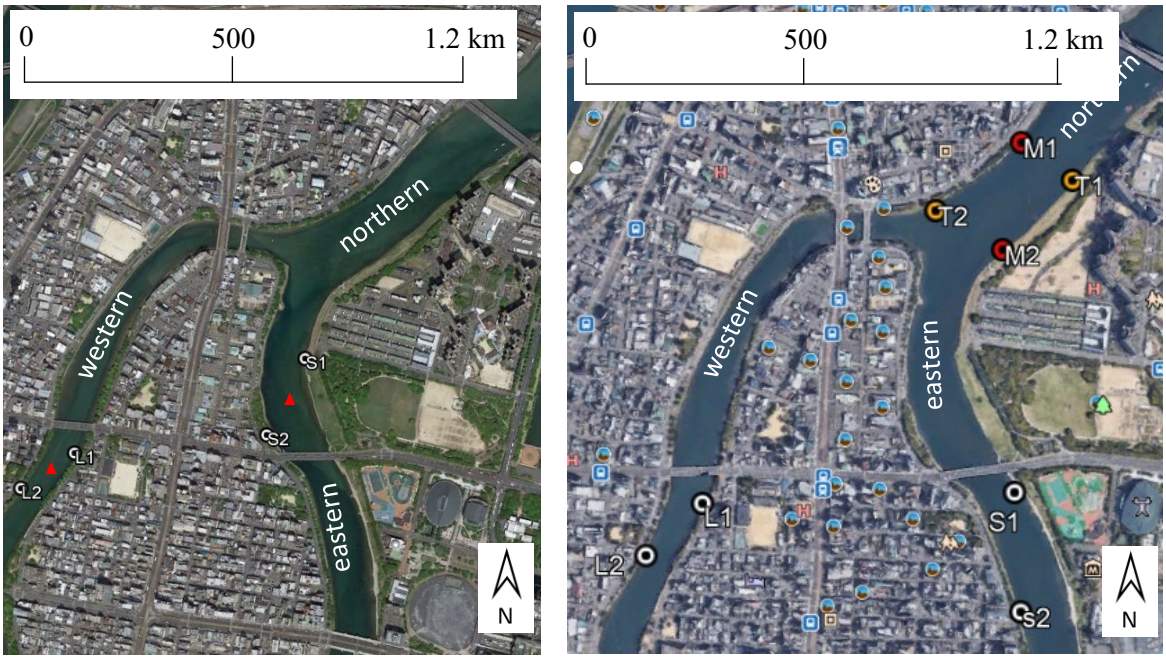

Figure 5.1. Study area of experiment sites in : (left) 2016 (right) 2017. S1-S2, L1-L2, and M1-M2, T1-T2, represent location of transducers of FATS in eastern and western branches, respectively. Water level and C-T sensors attached at M1, S2 and L2. The two red triangles represent ADCP-Aquadopp.

5.2.2. Velocity and salinity measurements using FATS

The FATS observations were conducted in two periods, i.e., June and August 2016, and June 2017. In 2016, two couples of FATS has been deployed in two branches, i.e., western and eastern branches, using 52-kHz FATS and 30-kHz FATS, respectively, as shown in Figure 5.1 (left column). In 2017, three couples of FATS has been deployed in three banches, i.e., northern, eastern and western, as shown in Figure 5.1 (right column). The frequency was

selected in accordance with the river width, smaller western branch needed higher frequency to ensure a sufficient velocity resolution. The cross-sectional average velocitiy in the direction of stream flow (v) is estimaetd by the following equation [29, 52].

$$v = u_m / \cos\theta \tag{5.1}$$

where u_m is mean velocity along ray path, and θ is angle between the ray path and streamline.

To estimate the cross-sectional average salinity in the tidal estuary using FATS, Medwin equation is used, as follows [52, 53].

$$S = 35 + (c - 1449.2 - 4.6T + 0.055T^2 - 0.00029T^3 - 0.016D)/(1.34 - 0.01T) \tag{5.2}$$

where c, T and D are sound velocity, temperature, and depth, respectively. This equation is valid if $0 \leq T \leq 35$ºC, $0 \leq S \leq 45$ ppt and $0 \leq D \leq 1000$ m. The salinities data from C-T sensor will be used as a reference. The author deployed the FATS in the eastern, western, and northern branches. Therefore, in order to cover salinity monitoring in three channels that connected to the junction, three C-T sensors were deployed in each channel.

5.2.3. ADCP measurement campaigns

To provide and establish reference velocity data for validating FATS and numerical model, moored 2MHz-ADCP campaigns were conducted. At the middle of transmission line of FATS, between transducers, the author deployed upward looking ADCP with deployment planning 600 s profile interval, 0.1 m cell size, 300 s average interval and 0.1 m blanking distance. ADCP provided velocity data, tidal level record, and current direction. ADCP measurements were conducted in June and August 2016. Owing to several problems in relation of missing data of FATS in June and August 2016, only short data was used to verification.

5.2.4. RMA 2 for modeling 2D velocity distributions at a tidal channel junction

The numerical model implemented in this study is RMA2 (resource modeling associates) which is part of surface water modeling system (SMS). The RMA2 is used to simulate the velocity and tidal wave. The RMA2 is two-dimensional finite element model to solve the depth-integrated equation of fluid mass and momentum conservation in two horizontal directions, as follows [62].

$$h\frac{\partial u}{\partial t} + hu\frac{\partial u}{\partial x} + hv\frac{\partial u}{\partial y} - \frac{h}{\rho}\left[E_{xx}\frac{\partial^2 u}{\partial x^2} + E_{xy}\frac{\partial^2 u}{\partial y^2}\right] + gh\left[\frac{\partial a_b}{\partial x} + \frac{\partial h}{\partial x}\right] + \frac{gun^2}{\left(1.486\, h^{\frac{1}{6}}\right)^2}(u^2+v^2)^{\frac{1}{2}} - \zeta V_a^2 \cos\psi_w - 2hv\omega_r \sin\Phi_l = 0 \quad (5.3\text{ a})$$

$$h\frac{\partial v}{\partial t} + hu\frac{\partial v}{\partial x} + hv\frac{\partial v}{\partial y} - \frac{h}{\rho}\left[E_{yx}\frac{\partial^2 v}{\partial x^2} + E_{yy}\frac{\partial^2 v}{\partial y^2}\right] + gh\left[\frac{\partial a_b}{\partial y} + \frac{\partial h}{\partial y}\right] + \frac{gvn^2}{\left(1.486\, h^{\frac{1}{6}}\right)^2}(u^2+v^2)^{\frac{1}{2}} - \zeta V_a^2 \sin\psi_w - 2hu\omega_r \sin\Phi_l = 0 \quad (5.3\text{ b})$$

$$\frac{\partial h}{\partial t} + h\left(\frac{\partial u}{\partial x} + \frac{\partial v}{\partial y}\right) + u\frac{\partial h}{\partial x} + v\frac{\partial h}{\partial y} = 0 \quad (5.3\text{ c})$$

where :

h = Water depth
u,v = Velocities in the Cartesian directions
x,y,t = Cartesian coordinates and time
ρ = Density of fluid
E = Eddy viscosity coefficient
g = Acceleration due to gravity
a_b = elevation of bottom
n = Manning's roughness n-value
ζ = Empirical wind shear coefficient
V_a = wind speed
ψ_w = wind direction
ω_r = Speed of earth's angular rotation
Φ_l = Local latitude

The density of water in the RMA 2 is determined as properties of water. In this study, for the estuaries, the density of water in this numerical model uses the saltwater density (ρ = 1024 kg/m^3). Geometry and bathymetry of channel network data were obtained from the Ministry of

Land, Infrastructure, Transport, and Tourism (MLIT). Figure 5.2. shows a mesh of the calculation domain of Ota River estuary, which consists of 9453 elements and 25736 nodes. The dimension of the calculation domain is approximately 3 km x 7 km. Three different color points in each branch were used to calculate tidal velocity to be compared with ADCP data.

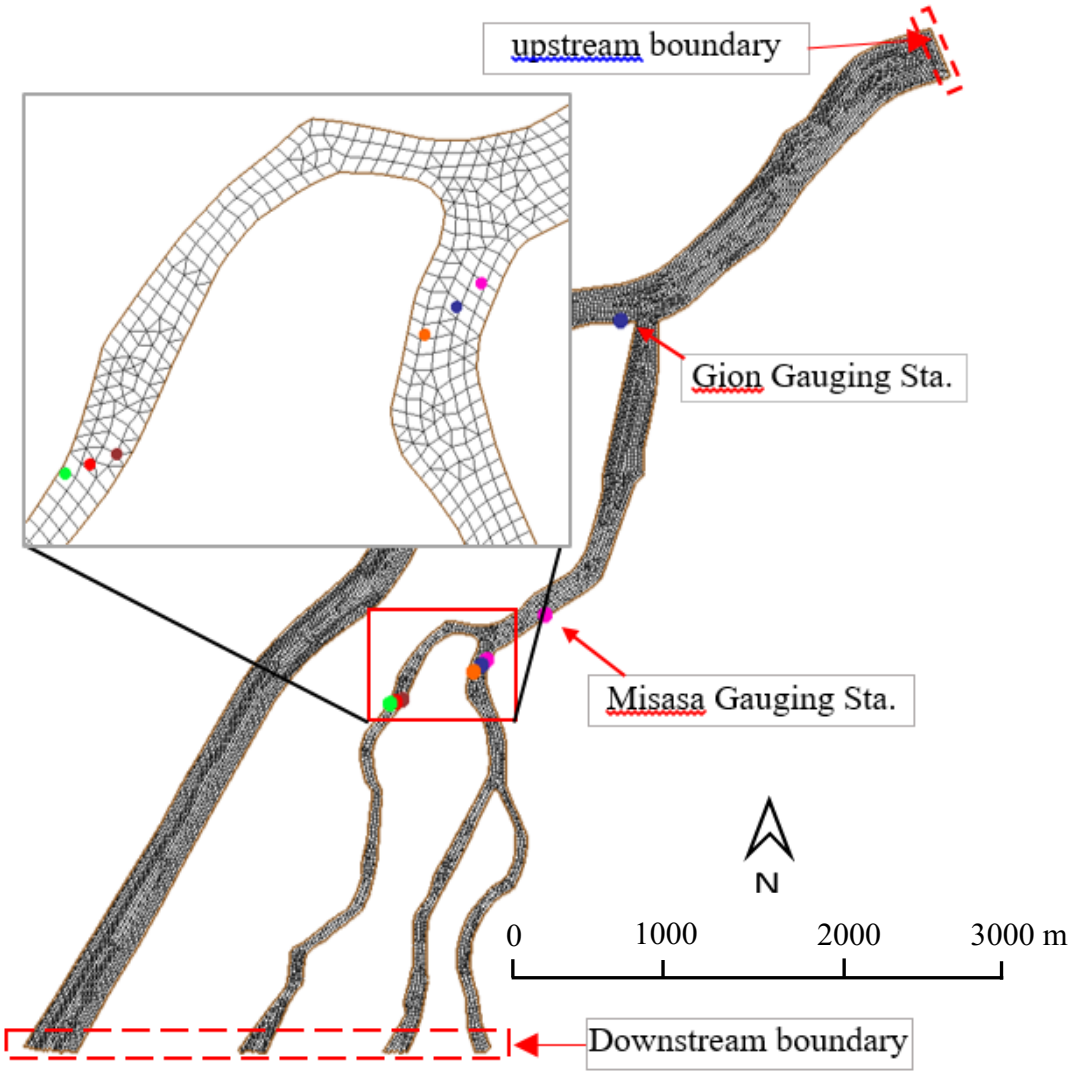

Figure 5.2. Mesh of calculation domain. The different color points represent observation points of computed values from RMA2 results.

The boundary conditions of the upstream and downstream are typically assigned discharge and water level, respectively. The boundary condition for the discharge input as nodal along the edge of an element at the upstream boundary. Similarly, the boundary condition for the

water level in the downstream also input as nodal along the edge of an element at the downstream boundary [62].

Several adjustments such as the Manning roughness coefficient (n) and turbulent exchange coefficient (E) are needed to get a good agreement between model and observation [63]. Computed and observed water level and velocity are provided and also compared by scatter plots of computed versus observed data with linear regression statistics.

5.3. Application of FATS for measuring flow velocity during high and normal flow condition

Figure 5.3 (top row) demonstrates the application of FATS to calculate the tidal velocity at the eastern branch during high flow condition in June 2016. However, the author cannot continuously measure velocity using FATS after flood event due to the missing data. Similarly, Figure 5.3 (bottom row) shows the temporal variation of tidal velocity at the western branch during normal flow condition in August 2016.

The tidal velocity measured by FATS shows different result compared to the ADCP result. These differences occur because FATS calculates the velocity based on the cross-sectional average velocity, whereas ADCP uses depth-averaged calculation which is based on the one point measurement. The other reason, ADCP deployed in the middle of the river which is the depth is shallow, whereas FATS is deployed in the deeper part of the river [64].

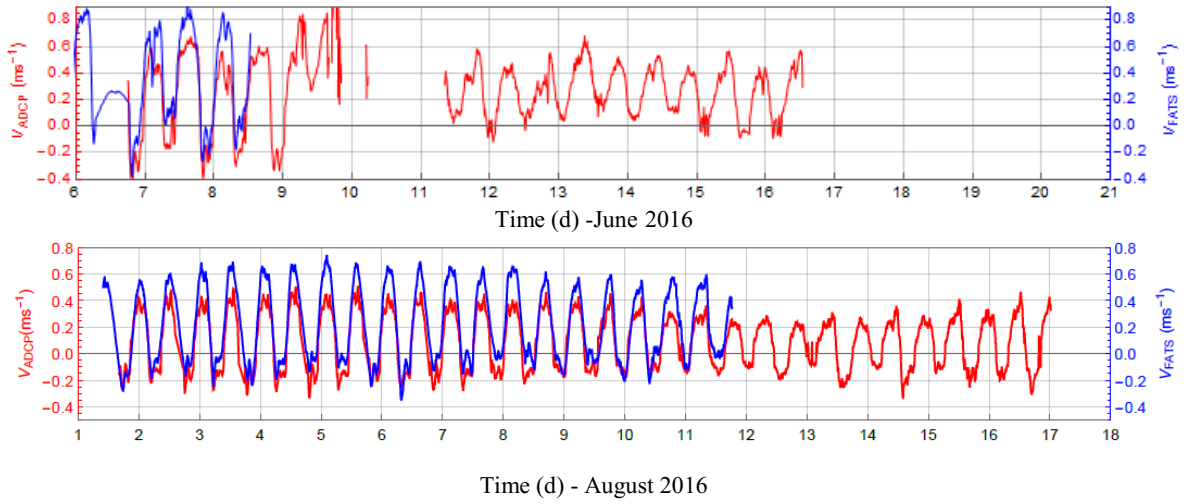

Figure 5.3. Comparison of the velocity profile between: (top) ADCP and FATS at the eastern branch during high flow condition; (bottom) ADCP and FATS at the western branch during normal flow condition. The FATS and ADCP results are represented by the blue and red lines, respectively.

5.4. Application of FATS for measuring salinity at a tidal channel junction

Figure 5.4 shows the salinity estimated by FATS at the eastern branch in 2016. It can be confirmed that FATS estimates seem reasonable compared to the C-T sensor estimates. There are negative values of FATS and the gap between FATS and CT-sensor results, particularly during the ebb tide, because several reasons: (i) transducers were dried out during the ebb tide, thus cannot measure salinity profile properly; (ii) C-T sensor is one point measurement and FATS is cross-sectional averaged salinity; (iii) The ray length of FATS changes due to the tide. Estimating the salinity using FATS is highly sensitive to the relative error of ray length [50].

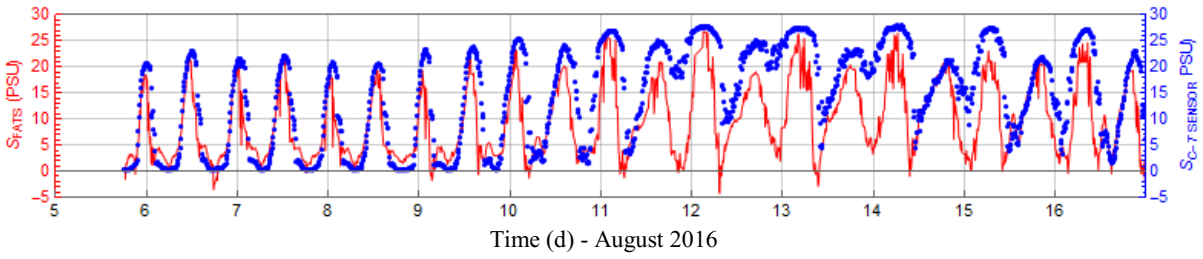

Figure 5.4. Salinity comparison in eastern branch between FATS and C-T sensor. The blue and red lines color represent the C-T sensor and FATS, respectively.

In 2017, three couples of FATS were deployed in three branches connected to a tidal channel junction from 5 to 27 June as shown in Figure 5.1. (right column). Due to the different days of FATS deployment and missing data, the length of FATS data differs in each branch. Figure 5.5 shows the temporal variation of salinity measured by FATS in three branches, i.e., northern, eastern, and western, respectively.

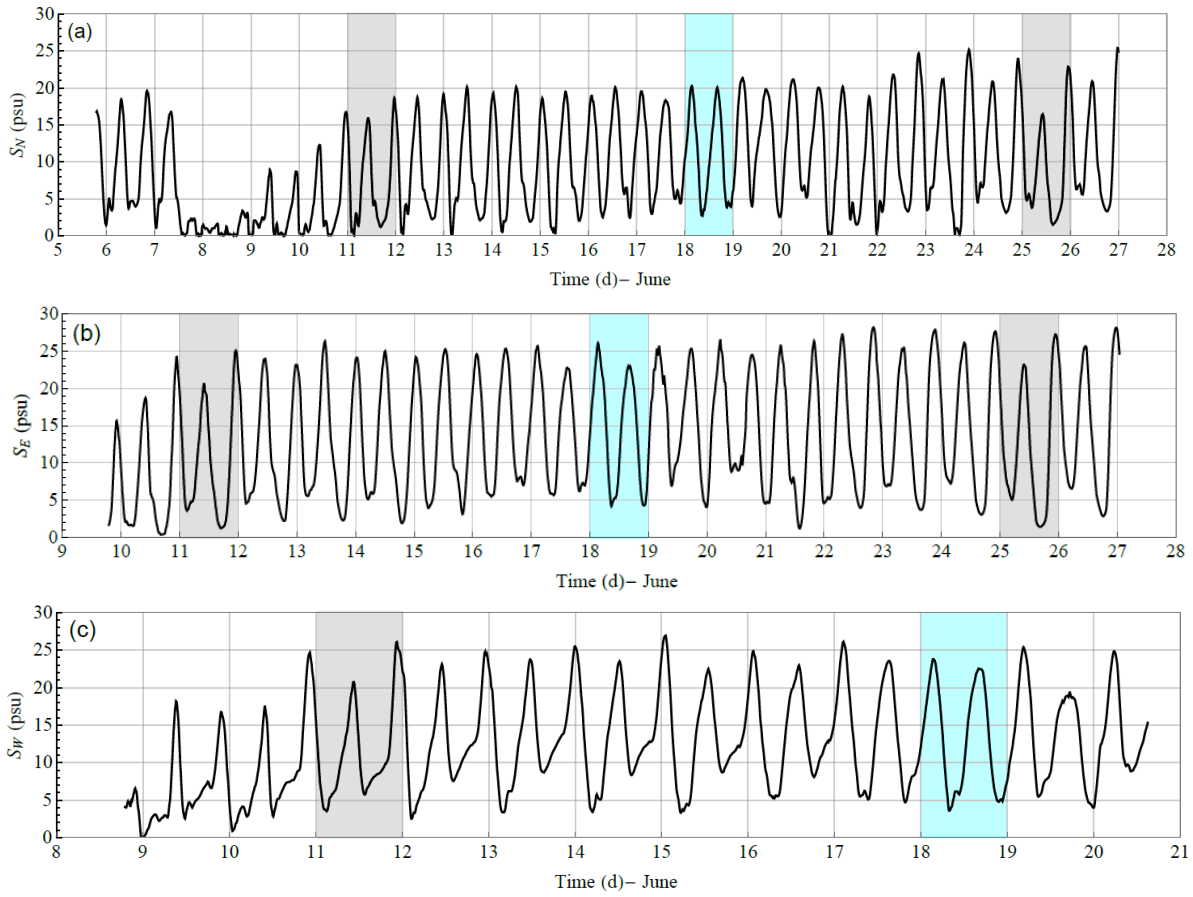

Figure 5.5. Temporal variation of salinity in (a) northern branch (b) eastern branch; (c) western branch. The grey and blue color box represent the spring and neap tide, respectively.

Figure 5.5. (a) shows the effect of heavy rain from 7 to 8 June 2017 which can diminish the salinity and its effect still influences the salinity behavior from 9 to 10 June 2017. To quantify the salinity in three branches, the author calculates the subtidal salinity by applying the low-pass filter to remove the tidal effect as shown in Figure 5.6. It can be seen that the subtidal salinity at the northern branch is smaller than at the eastern and western branches,

irrespective of the tidal range. The temporal variation of subtidal salinity in the eastern and western branches are almost equal without relation to the tidal range.

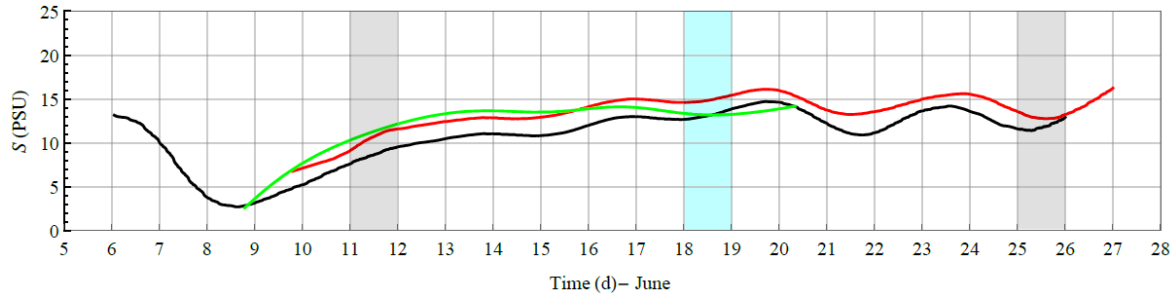

Figure 5.6. Subtidal salinity in three branches connected to a junction. The black, red, and green lines represent northern, eastern, and western branches, respectively. Grey and blue highlight represent the spring and neap tide, respectively.

5.5. Numerical simulation results of 2D velocity distributions between two seaward branches at the tidal channel junction

5.5.1. Calibration and verification

Calibration and validation are needed to obtain an optimize agreement between model and observed prototype data [62]. The time series of computed and observed water level shows good agreement as shown in Figure 5.7. The observed data were obtained from gauging stations (Misasa and Gion gauging stations). Further study is needed to apply the density in velocity simulation and to investigate the influence of density to the tidal wave propagation.

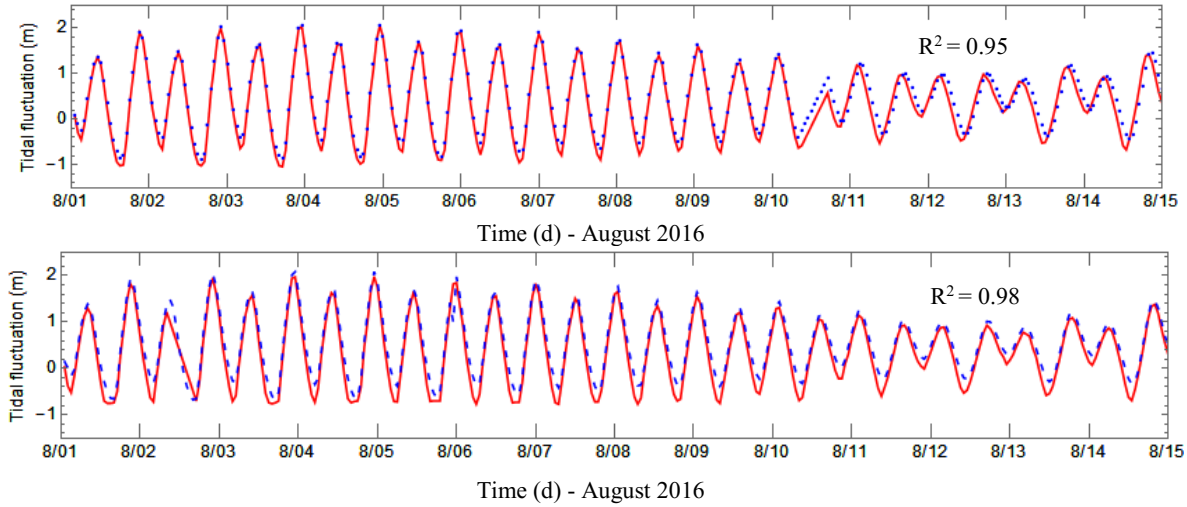

Figure 5.7. Comparison between computed and observed water level: (top) Misasa gauging station, (bottom) Gion gauging station. The computed and observed water levels are represented by blue dots and red line, respectively.

Verification is an attempt reproduction of a different set of prototype data without further adjustment [62]. Figure 5.8 (top row) shows the comparison of the velocity profile at the eastern branch from 11 to 16 June 2016 obtained from ADCP (Aquadopp Profiler 2.0 MHZ) with the numerical model. Similarly, Figure 5.8 (bottom row) shows the temporal variation of tidal velocity at the western branch between ADCP and model result from 1 to 17 August 2016.

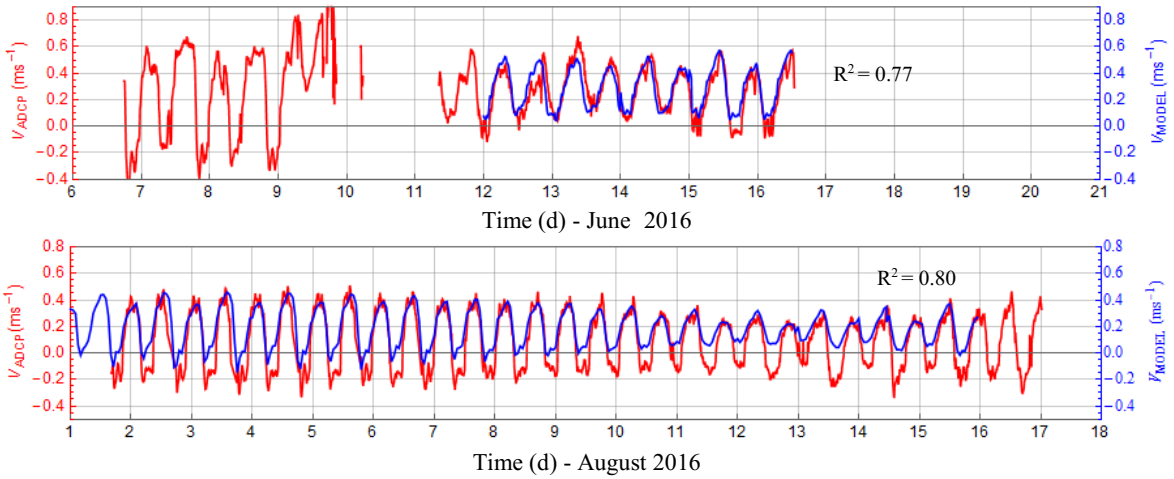

Figure 5.8. Comparison of velocity between ADCP and RMA2 model at: (top) eastern branch, (bottom) western branch. Positive velocity coincides with the seaward flow. The model and ADCP are represented by blue and red lines, respectively.

Based on the regression results, the good agreement cannot be achieved, but only satisfactory (R^2 between 0.77 – 0.80). However, the comparison of the numerical model with ADCP data was still considered reasonable. The model can simulate tidal velocity during ebb tide properly but tends to underestimate particularly during flood tide.

5.5.2. Numerical results of 2D velocity distributions at the channel junction

Figure 5.9. shows the flow velocity vectors at the tidal channel junction during the flood and ebb tide from 1 to 15 August 2016. It can be seen that the tidal velocity during the ebb tide is higher than that during the flood tide.

In addition, as presented in Figure 5.9 (top row), the water in the eastern branch flows into the western branch during the flood tide intermittently, as a result of the transfer of tidal energy from the eastern branch to the western branch. This happens due to the shorter branch of the eastern branch compared to the western branch [1].

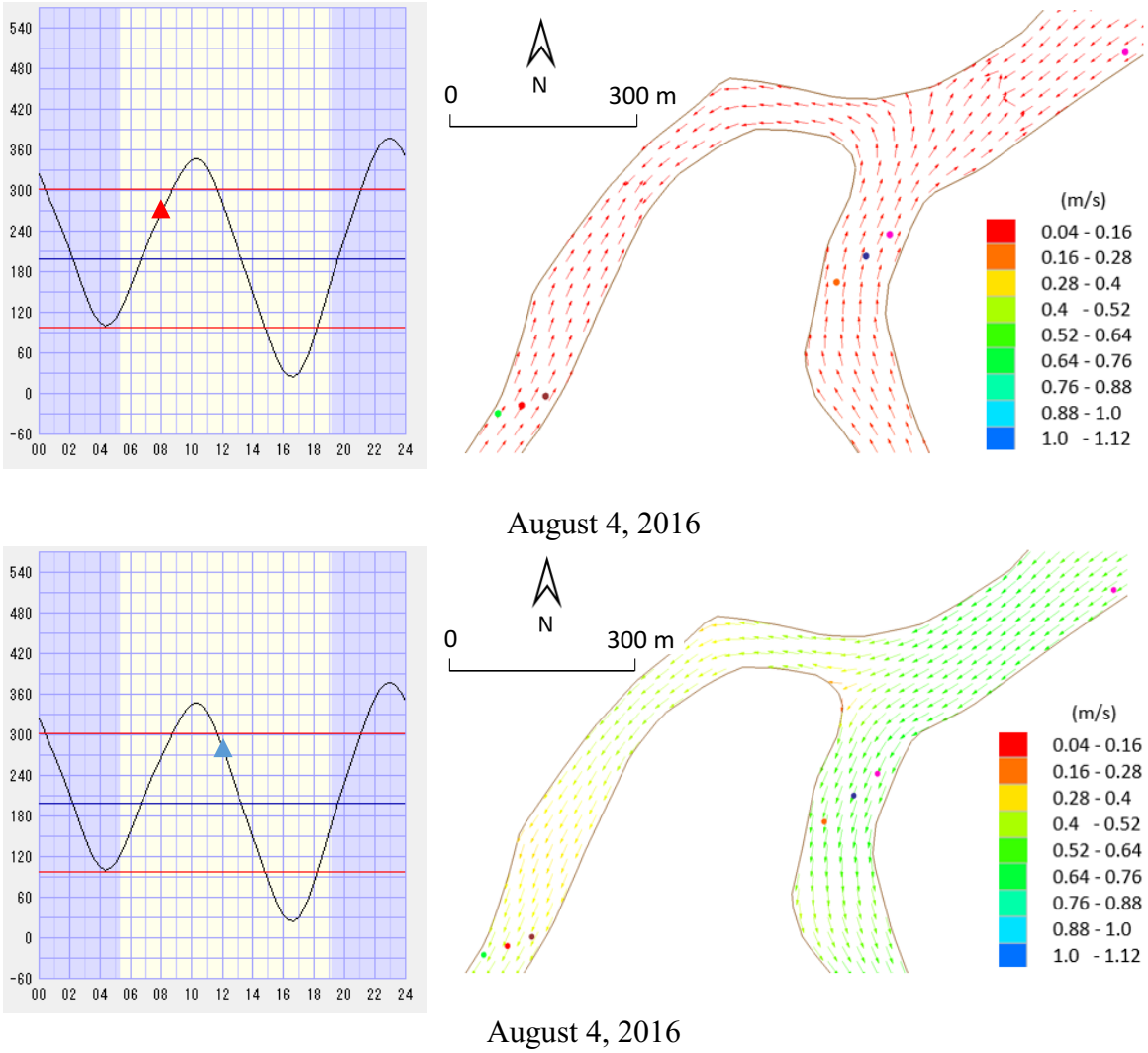

Figure 5.9. 2D velocity distribution during (top right) flood tide, (bottom right) ebb tide. The red and blue triangles represent the phase of flow velocity field during (top left) flood tide, (bottom left) ebb tide.

Based on the simulation results, the comparison of tidal velocity between two seaward branches at a tidal channel junction can be analyzed as shown in Figure 5.10, which denotes that the magnitude of flow velocity in the eastern branch is larger than at the western branch. In order to quantify the ratio of the velocity magnitude in the eastern and western branches, a low-pass filter was applied to remove tidal influence. The residual velocity at the eastern branch is estimated to be ~30 to ~43% larger than the velocity at the western branch.

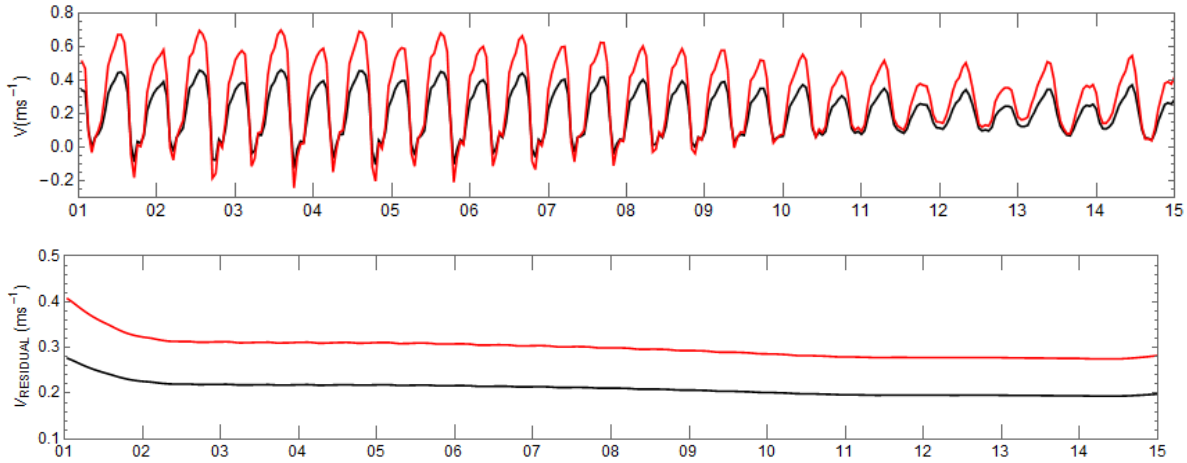

Figure 5.10 (top) Comparison of tidal velocity in eastern and western branches, (bottom) Residual velocities in the eastern and western branches. Positive velocity coincide with the seaward flow. The red and black lines represent the velocity at the eastern and western branches, respectively.

5.6. Conclusions

From this chapter, the author can demonstrate that the FATS has the ability to measure the temporal variation of tidal velocity during high flow condition (flood event) and normal flow condition and the temporal variation of cross-sectional average salinity.

The tidal velocity measured by FATS shows different result compared to the ADCP result. These differences occur because FATS calculates the velocity based on the cross-sectional average velocity, whereas ADCP uses depth-averaged calculation which is based on the one

point measurement. The other reason, ADCP deployed in the middle of the river which is the depth is shallow, whereas FATS is deployed in the deeper part of the river.

The subtidal salinity at the northern branch is smaller than at the eastern and western branches irrespective of the tidal range. The temporal variation of subtidal salinity in the eastern and western branches are almost equal without relation to the tidal range.

Numerical simulation results of flow velocity field at the tidal channel junction show that the velocity during ebb tide is stronger than during flood tide. In addition, the velocity at the eastern branch is higher than that at the western branch, which is consistent to the results of FATS as mentioned in section 3.

In addition, the water in the eastern branch flows into the western branch during the flood tide intermittently, as a result of the transfer of tidal energy from the eastern branch to the western branch. This happens due to the shorter branch of the eastern branch compared to the western branch.

Chapter 6. Concluding remarks and future work

6.1. Introduction

Although this study deals with the Ota River as a case-specific example, the presented results and discussion are not only aimed at demonstrating the dynamic of flow division and relationship between tidal discharge and water level at a junction, but also take advantage of utilizing the innovative hydro-acoustic system (FATS) for measuring discharge in high temporal resolution and exploring the hydrodynamic process at a tidal junction. Moreover, our findings should increase the knowledge for common hydrodynamic processes in multi-channel estuaries that have nearly similar environments over the world.

This study obtains the discharge and flow distribution data at a channel junction from the field experiment during more or less one month, which can capture the spring and neap tide variation. Temporal variations of tidal discharge were successfully measured by an innovative FATS instruments that deployed at three branches connected to a channel junction during a low-flow condition. The author uses two methods of FATS measurement to estimate discharge, i.e., index velocity method and two-crossed transmission lines.

The behavior of flow division between two seaward branches connected to a channel junction can be investigated during spring and neap tide variation. Thus, the influence during spring-neap tide on the flow division can be recognized. In addition, the temporal variation of the phase difference between the tidal discharge and water level at two seaward branches is also investigated.

The tidal velocity and subtidal salinity at a tidal channel junction were investigated using FATS. In addition, to simulate the 2D velocity distributions at a tidal channel junction, a 2D numerical model of RMA 2 is used.

6.2. Answering the research questions

6.2.1. Temporal variaiton of the tidal discharge and flow division at a tidal channel junction

To investigate the temporal variation of flow division between two seaward branches (eastern and western branches) that are connected to the tidal channel junction, the discharge asymmetry index for the maximum tidal discharge was used. There are three main questions:

a) What is the temporal variation of tidal discharge between two seaward branches, i.e., eastern and western branches?

The response of tidal dynamic to the local geometry between two seaward branches shows distinct characteristics, where the asymmetric discharge at the western branch is more pronounced compared with that at the eastern branch. The asymmetric tidal discharge observed at the western branch indicates the ebb discharge is larger than the flood discharge. On the contrary, the characteristic of tidal discharge at the eastern branch is nearly equal during the ebb and flood tide. The bathymetry of the western branch is shallower and narrower than the eastern branch. Therefore, the propagating tidal wave in shallow and narrow branches, and modulated with the river discharge, can generate the nonlinear effect as a result of interaction with the local topography. This nonlinear effect leads to the generation and development of shallow-water constituents, which cause tidal distortion and asymmetry. This asymmetric tidal discharge can induce a seaward sediment movement.

b) What is the temporal variation of flow division between two seaward branches (eastern and western branches)?

The discharge asymmetry index ranges from −0.02 to 0.26 during the 10 to 21 June, suggesting that the eastern branch has the capability to deliver greater amounts of subtidal

discharge, approximately 55%–63% compared with the western branch. However, the flow division is nearly equal during the neap tide.

c) How do the spring and neap tide affect the tidal discharge division?

The effect of spring and neap tide on the tidal discharge division is not clear. The temporal variation of subtidal discharge in the western branch is relatively constant, while in the eastern branch the temporal variation of subtidal discharge is relatively varied.

The equality of the asymmetry index between the eastern and western channels can be observed clearly during the neap tide period. Nevertheless, the inequality of flow division is obviously prominent during the spring tide duration. This happen because the fluctuation in the subtidal discharge at the eastern branch is greater than that at the western branch; the subtidal discharge at the eastern branch decreases during the neap tide, so that both subtidal discharges are nearly equal during the neap tide.

6.2.2. Temporal variation of the phase difference between the tidal discharge and water level at a tidal channel junction

Three main questions arise about the characteristic of phase difference at the junction:

a) Can the author compares the phase difference between the two seaward branches (the eastern and western branches)? As a follow up question, what is the dominant factor that influences the phase difference between the two seaward branches?

The wavelet analysis of the temporal variation of the phase differences between the two seaward branches shows slightly different behavior. Whereas a mimic standing wave characteristic ($\Delta\varphi = \sim 88.5°$) occurs at the western branch, a mixed wave characteristic ($\Delta\varphi = \sim 78°$) occurs at the eastern branch. It is shown that the phase difference between tidal discharge and the water level is relatively constant during the neap and spring tide. The discharge phase at the western branch leads the discharge phase at the eastern branch

by ~15 minutes. Additionally, the geometry analysis between the two seaward branches reveals that the western branch is more convergent compared to the eastern branch and therefore causes a larger phase difference at the junction. Thus, the convergence factor is more dominant compared to river discharge and bottom friction.

b) What is the behavior of phase difference at the landward branch of the junction (the northern branch)?

Using the same analysis, the author can say the phase difference between the tidal discharge and water level at the northern branch (landward branch of the junction) indicates a standing wave characteristic ($\Delta\varphi = \sim 90°$), which is slightly higher than the phase difference in the two seaward branches. This evidence implies that the phase difference is slightly increased after passing through the junction into the northern branch. Further study is needed to explore the characteristics of the phase difference in the larger area of the multi-channel estuary.

c) Is the phase difference influenced by the spring and neap tide?

The phase difference between two seaward branches changes slightly during the spring and neap tide. The phase difference between the tidal discharge and water level is relatively constant, where during the spring tide, the phase difference is ~11°, whereas during the neap tide, the phase difference is ~9°. Therefore, the change of the phase difference between the spring and neap tide is not significant. This phenomenon is probably because the phase difference is a function of a ratio between bank convergence and tidal wavelength. Moreover, the phase difference can be affected by two factors, that is, the river discharge and topography of the estuarine channel, also known as estuary shape.

6.2.3. Investigation of flow velocity and salinity using FATS and simulation of 2D velocity distributions at a channel junction using a 2D numerical model

To investigate the dynamics of tidal velocity and salinity at the channel junction are of paramount importance for the maintenance of channels, water usage, and the estuarine management. There are three main questions as follows.

a) How is the temporal variation of tidal velocity at a tidal channel junction measured by FATS during high flow and normal flow condition?

The FATS can estimate the temporal variation of tidal velocity during high flow condition and normal flow condition. The tidal velocity measured by FATS shows different result compared to the ADCP result. These differences occur because FATS calculates the velocity based on the cross-sectional average velocity, whereas ADCP uses depth-averaged calculation which is based on the one point measurement. The other reason, ADCP deployed in the middle of the river which is the depth is shallow, whereas FATS is deployed in the deeper part of the river.

b) How is the temporal variation of subtidal salinity at a tidal channel junction measured by FATS?

The temporal variation of subtidal salinity at the northern branch is smaller than at the eastern and western branches irrespective of the tidal range. The temporal variation of subtidal salinity in the eastern and western branches are almost equal without relation to the tidal range.

c) How is the 2D velocity distributions at a tidal channel junction during flood and ebb tide?

Numerical results of tidal velocity at the tidal junction show that the tidal velocity at the eastern branch is higher than that at the western branch. In addition, to quantify the ratio of the residual velocity magnitude between the eastern and western branches, a low-pass

filter was applied. The residual velocity at the eastern branch is estimated to be ~30 to ~43% larger than the velocity at the western branch.

The water in the eastern branch flows into the western branch during the flood tide intermittently, as a result of the transfer of tidal energy from the eastern branch to the western branch. This happens due to the shorter branch of the eastern branch compared to the western branch.

6.3. Recommendation for future works

The works which can be explored in the future can be explained as follows:

a. To elucidate mechanism that cause the changing subtidal discharge.

During spring tide, the subtidal discharge in the eastern branch tends to be higher compared to the subtidal discharge in the western branch. The mechanism that cause the changing subtidal discharge during spring and neap tide is still not clear. Some questions that arise, as follows:

-Why the subtidal discharge in the western branch is relatively constant compared to the subtidal discharge in the eastern branch along the studied period?

-Why the subtidal discharge tends to decrease during the neap tide?

In order to study the mechanism which causes the changing subtidal discharge, probably continuously monitoring tidal discharge during high-flow condition and seasonal variation are needed. Furthermore, deploying the several FATS system in different location between two branches to investigate the dynamic behavior of subtidal discharge.

b. To explore the characteristics of the phase difference in the larger area of the multi-channel estuary.

Investigation of dynamic behavior of phase difference in this present study particularly only focus on the two seaward branches connected to a tidal channel junction. In order to understand comprehensively the dynamic behavior of phase difference along the channel junction, investigating the phase difference in all branches is needed, starting from the river mouth to the tidal channel junction.

Appendix

This dissertation contains of several publications, as follows.

1. Refereed publication:
    a. Danial, M.M.; Kawanisi, K.; Motlagh, M. B.; Al Sawaf, M.B.; Wakabayasi, T. (2017). **Investigation of Flow Velocity and Salinity Behavior in Ota River Estuary Using Acoustic Tomography Method and Numerical Modeling**, Journal of Japan Society of Civil Engineers, Ser. B1 (Hydraulic Engineering), 73(4), I_1033–I_1038.
    b. Danial, M.M.; Kawanisi, K.; Al Sawaf, M.B. (2019). **Characteristics of Tidal Discharge and Phase Difference at a Tidal Channel Junction Investigated Using the Fluvial Acoustic Tomography System**. *Water (IF: 2.524)*, *11(4)*, 857–877. https://doi.org/10.3390/w11040857
2. Conference presentation:
    a. Mochammad Meddy Danial, Kiyosi Kawanisi, Masoud Bahraini Motlagh, Mohamad Basel Al Sawaf, Junya Kagami, (2017). **Monitoring of continuous tidal current pattern in asymmetric bifurcation channel network using acoustic tomography method and numerical modeling**, paper presented at the 37th IAHR World Congress, Kuala Lumpur, August 13-18.

References

1. Buschman, F. A.; Hoitink, A. J. F.; Van Der Vegt, M.; Hoekstra, P. Subtidal flow division at a shallow tidal junction. *Water Resour. Res.* **2010**, *46*, 1–12, doi:10.1029/2010WR009266.
2. Sassi, M. G.; Hoitink, A. J. F.; de Brye, B.; Vermeulen, B.; Deleersnijder, E. Tidal impact on the division of river discharge over distributary channels in the Mahakam Delta. *Ocean Dyn.* **2011**, *61*, 2211–2228, doi:10.1007/s10236-011-0473-9.
3. Zhang, W.; Feng, H.; Hoitink, A. J. F.; Zhu, Y.; Gong, F. Estuarine , Coastal and Shelf Science Tidal impacts on the subtidal fl ow division at the main bifurcation in the Yangtze River Delta. *Estuar. Coast. Shelf Sci.* **2017**, *196*, 301–314, doi:10.1016/j.ecss.2017.07.008.
4. Horrevoets, A. C.; Savenije, H. H. G.; Schuurman, J. N.; Graas, S. The influence of river discharge on tidal damping in alluvial estuaries. *J. Hydrol.* **2004**, *294*, 213–228, doi:10.1016/j.jhydrol.2004.02.012.
5. Savenije, H. H. G.; Veling, E. J. M. Relation between tidal damping and wave celerity in estuaries. **2005**, *110*, 1–10, doi:10.1029/2004JC002278.
6. Savenije, H. H. G.; Toffolon, M.; Haas, J.; Veling, E. J. M. Analytical description of tidal dynamics in convergent estuaries. *J. Geophys. Res.* **2008**, 1–27, doi:10.1029/2007JC004408.
7. Leonardi, N.; Kolker, A. S.; Fagherazzi, S. Advances in Water Resources Interplay between river discharge and tides in a delta distributary. *Adv. Water Resour.* **2015**, *80*, 69–78, doi:10.1016/j.advwatres.2015.03.005.
8. Sassi, M. G.; Hoitink, A. J. F.; De Brye, B.; Vermeulen, B.; Deleersnijder, E. Tidal impact on the division of river discharge over distributary channels in the Mahakam Delta. *Ocean Dyn.* **2011**, *61*, 2211–2228, doi:10.1007/s10236-011-0473-9.

9. Buschman, F. A.; Van Der Vegt, M.; Hoitink, A. J. F.; Hoekstra, P. Water and suspended sediment division at a stratified tidal junction. *J. Geophys. Res. Ocean.* **2013**, *118*, 1459–1472, doi:10.1002/jgrc.20124.

10. Cai, H.; Savenije, H. H. G.; Toffolon, M. A new analytical framework for assessing the effect of sea-level rise and dredging on tidal damping in estuaries. *J. Geophys. Res.* **2012**, *117*, 1–20, doi:10.1029/2012JC008000.

11. Cameron, W. M.; Pritchard, D. W. *Estuaries*; Hill, M. N., Ed.; John Wiley and Sons: New York, 1963; Vol. 2;.

12. Perillo, G. M. M. Chapter 2 Definitions and Geomophologic Classifications of Estuaries. In *Developments in Sedimentology*; Perillo, G. M. E., Ed.; Elsevier: Amsterdam, 1995; Vol. 53, pp. 17–47 ISBN 978-0-444-88170-0.

13. Savenije, B. H. H. G. *Salinity and tides in fluvial estuaries*; -, Ed.; 1st ed.; Elsevier Science: Amsterdam, 2005; ISBN 9780444521088.

14. Tessier, B. *Stratigraphy of Tide-Dominates Estuaries*; Davis, R. A., Dalrymple, R. W., Eds.; 1st ed.; Springer: Netherland, 2012; ISBN 9789400701236.

15. Pittaluga, M. B.; Tambroni, N.; Canestrelli, A.; Slingerland, R.; Lanzoni, S.; Seminara, G. Journal of Geophysical Research : Earth Surface Where river and tide meet : The morphodynamic equilibrium of alluvial estuaries. *J. Geophys. Res. Earth Surf.* **2014**, doi:10.1002/2014JF003233.Received.

16. Davies, J. L. A Morphogenetic Approach to World Shorelines. *Zeitschrift fur Geomorphol.* **1964**, *8*, 127–142.

17. Friedrichs, C. T.; Aubrey, D. G. Tidal propagation in strongly convergent channels. *J. Geophys. Res.* **1994**, *99*, 3321–3336, doi:10.1029/93JC03219.

18. Sassi, M. G.; Hoitink, A. J. F.; De Brye, B.; Deleersnijder, E. Downstream hydraulic geometry of a tidally influenced river delta. *J. Geophys. Res. F Earth Surf.* **2012**, *117*,

1–13, doi:10.1029/2012JF002448.

19. Jay, D. A.; Flinchem, P. Interaction of fluctuating river flow with a barotropic tide: A demonstration of wavelet tidal analysis methods. *J. Geophys. Res.* **1997**, *102*, 5705–5720, doi:10.1029/96JC00496.

20. Buschman, F. A.; Hoitink, A. J. F.; Van Der Vegt, M.; Hoekstra, P. Subtidal water level variation controlled by river flow and tides. *Water Resour. Res.* **2009**, *45*, 1–12, doi:10.1029/2009WR008167.

21. Jay, D. A. Green's law revisited: Tidal long-wave propagation in channels with strong topography. *J. Geophys. Res.* **1991**, *96*, 20585, doi:10.1029/91JC01633.

22. Stive, M. J. F.; Rakhorst, R. D. Review of empirical relationships between inlet cross-section and tidal prism. *J. Water Resour. Environ. Eng.* **2008**, *23*, 89–95.

23. Alebregtse, N. C.; de Swart, H. E. Effect of river discharge and geometry on tides and net water transport in an estuarine network, an idealized model applied to the Yangtze Estuary. *Cont. Shelf Res.* **2016**, *123*, 29–49, doi:10.1016/j.csr.2016.03.028.

24. Lu, S.; Tong, C.; Lee, D. .; Zheng, J.; Shen, J.; Zhang, W.; Yan, Y. Propagation of tidal waves up in Yangtze Estuary during the dry season. *J. Geophys. Res. Ocean.* **2015**, *120*, 6445–6473, doi:10.1002/2014JC010414.

25. Guo, L.; Van Der Wegen, M.; Jay, D. A.; Matte, P.; Wang, Z. B.; Roelvink, D.; He, Q. River-tide dynamics: Exploration of nonstationary and nonlinear tidal behavior in the Yangtze River estuary. *J. Geophys. Res. C Ocean.* **2015**, *120*, 3499–3521, doi:10.1002/2014JC010491.

26. Nguyen, A. D. *SALT INTRUSION , TIDES AND MIXING IN MULTI-CHANNEL ESTUARIES*; Taylor & Francis/Balkema: The Netherlands, 2008; ISBN 9780415471220.

27. Wang, Z. B.; Ding, P. X. The Branching Channel Network in The Yangtze Estuary. In

Coastal Engineering Proceedings; Lynett, P., Smith, J. M., Eds.; ASCE: Spain, 2012; Vol. 33, pp. 1–12.

28. Edmonds, D. A.; Slingerland, R. L. Stability of delta distributary networks and their bifurcations. *Water Resour. Res.* **2008**, *44*, 1–13, doi:10.1029/2008WR006992.
29. Gotoh, T.; Fukuoka, S.; Tanaka, R. *Evaluation of flood discharge hydrographs and bed variations in a channel network on the Ota River delta ,*; Chavoshian, A., Takeuchi, K., Eds.; 357th ed.; IAHS: Wallingford, Oxfordshire, 2013; ISBN 9781907161353.
30. Hoitink, A. J. F.; Buschman, F. A.; Vermeulen, B. Continuous measurements of discharge from a horizontal acoustic Doppler current profiler in a tidal river. *Water Resour. Res.* **2009**, *45*, 1–13, doi:10.1029/2009WR007791.
31. Garel, E.; D'Alimonte, D. Continuous river discharge monitoring with bottom-mounted current profilers at narrow tidal estuaries. *Cont. Shelf Res.* **2017**, *133*, 1–12, doi:10.1016/j.csr.2016.12.001.
32. Laenen, A.; Smith, W. Acoustic Systems for the Measurement of Streamflow. *Water-Supply Pap. 2213, USGS, Washington, DC* **1983**.
33. Chen, Mi.; Kaneko, A.; Lin, J.; Zhang, C. Mapping of a Typhoon-Driven Coastal Upwelling by Assimilating Coastal Acoustic Tomography Data. *J. Geophys. Res. Ocean.* **2017**, 7822–7837, doi:10.1002/2017JC012812.
34. Kawanisi, K.; Razaz, M.; Yano, J.; Ishikawa, K. Continuous monitoring of a dam flush in a shallow river using two crossing ultrasonic transmission lines. *Meas. Sci. Technol.* **2013**, *24*, 055303, doi:10.1088/0957-0233/24/5/055303.
35. Kawanisi, K.; Al Sawaf, M. B.; Danial, M. M. Automated real-time stream flow acquisition in a mountainous river using acoustic tomography. *J. Hydrol. Eng.* **2018**, *23*, 1–7, doi:10.1061/(ASCE)HE.1943-5584.0001604.

36. Muste, M.; Fujita, I.; Hauet, A. Large-scale particle image velocimetry for measurements in riverine environments. *Water Resour. Res.* **2008**, *44*, 1–14, doi:10.1029/2008WR006950.

37. Nihei, Y.; Kimizu, A. A new monitoring system for river discharge with horizontal acoustic Doppler current profiler measurements and river flow simulation. *Water Resour. Res.* **2008**, *44*, 1–15, doi:10.1029/2008WR006970.

38. Chen, Y. C. Flood discharge measurement of a mountain river-Nanshih River in Taiwan. *Hydrol. Earth Syst. Sci.* **2013**, *17*, 1951–1962, doi:10.5194/hess-17-1951-2013.

39. Mueller, D. S.; Wagner, C. R. *Measuring Discharge with Acoustic Doppler Current Profilers from a Moving Boat: U.S. Geological Survey Techniques and Methods 3A–22, 72 p.*; 2009;

40. Costa, J. E.; Cheng, R. T.; Haeni, F. P.; Melcher, N.; Spicer, K. R.; Hayes, E.; Plant, W.; Hayes, K.; Teague, C.; Barrick, D. Use of radars to monitor stream discharge by noncontact methods. *Water Resour. Res.* **2006**, *42*, 1–14, doi:10.1029/2005WR004430.

41. Sloat, J.; Gain, W. Application of acoustic velocity meters for gaging discharge of three low-velocity tidal streams in the St. Johns River Basin, Northeast Florida. *US Geol. Surv. Water-Resources Investig. Rep. 95-4230* **1995**, 26.

42. Razaz, M.; Kawanisi, K.; Nistor, I.; Sharifi, S. An acoustic travel time method for continuous velocity monitoring in shallow tidal streams. *Water Resour. Res.* **2013**, *49*, 4885–4899, doi:10.1002/wrcr.20375.

43. Bahreinimotlagh, M.; Kawanisi, K.; Danial, M. M.; Al Sawaf, M. B.; Kagami, J. Application of shallow-water acoustic tomography to measure flow direction and river discharge. *Flow Meas. Instrum.* **2016**, *51*, 30–39, doi:10.1016/j.flowmeasinst.2016.08.010.

44. Kawanisi, K.; Bahrainimotlagh, M.; Al Sawaf, M. B.; Razaz, M. High-frequency streamflow acquisition and bed level/flow angle estimates in a mountainous river using shallow-water acoustic tomography. *Hydrol. Process.* **2016**, *30*, 2247–2254, doi:10.1002/hyp.10796.

45. Brophy, L.; van de Wetering, S. *Ni-les'tun tidal wetland restoration effectiveness monitoring : Baseline (2010-2011)*; 2012;

46. Kempema, E.; Stiver, J.; Ettema, R. *Effects of Warm CBM Product Water Discharge on Winter Fluvial and Ice Processes in the Powder River Basin*; 2010;

47. Sassi, M. G.; Hoitink, A. J. F.; Vermeulen, B.; Hidayat, H. Discharge estimation from H-ADCP measurements in a tidal river subject to sidewall effects and a mobile bed. *Water Resour. Res.* **2011**, *47*, 1–14, doi:10.1029/2010WR009972.

48. Levesque, V. A.; Oberg, K. A. Computing Discharge Using the Index Velocity Method. *U.S. Geol. Surv. Tech. Methods 3–A23* **2012**, 148.

49. Hidayat, H.; Hoitink, A. J. F.; Sassi, M. G.; Torfs, P. J. J. F. Prediction of Discharge in a Tidal River Using Artificial Neural Networks. *J. Hydrol. Eng* **2014**, *19*, 1–8, doi:10.1061/(ASCE)HE.1943-5584.

50. Kawanisi, K.; Razaz, M.; Kaneko, A.; Watanabe, S. Long-term measurement of stream flow and salinity in a tidal river by the use of the fluvial acoustic tomography system. *J. Hydrol.* **2010**, *380*, 74–81, doi:10.1016/j.jhydrol.2009.10.024.

51. Danial, M. M.; Kawanisi, K.; Al Sawaf, M. B. Characteristics of tidal discharge and phase difference at a tidal channel junction investigated using the fluvial acoustic tomography system. *Water (Switzerland)* **2019**, *11*, doi:10.3390/w11040857.

52. Savenije, H. H. G.; Veling, E. J. M. Relation between tidal damping and wave celerity in estuaries. *J. Geophys. Res.* **2005**, *110*, 1–10, doi:10.1029/2004JC002278.

53. Gurley, K.; Kareem, A. Applications of wavelet transforms in earthquake, wind and

ocean engineering. *Eng. Struct.* **1999**, *21*, 149–167.

54. Lafrenière, M.; Sharp, M. Wavelet analysis of inter-annual variability in the runoff regimes of glacial and nival stream catchments, Bow Lake, Alberta. *Hydrol. Process.* **2003**, *17*, 1093–1118, doi:10.1002/hyp.1187.

55. Kim, B.; Jeong, H.; Kim, H.; Han, B. Exploring wavelet applications in civil engineering. *KSCE J. Civ. Eng.* **2017**, *21*, 1076–1086, doi:10.1007/s12205-016-0933-3.

56. Grinsted, A.; Moore, J. C.; Jevrejeva, S. Application of the cross wavelet transform and wavelet coherence to geophysical time series. *Nonlinear Process. Geophys.* **2004**, *11*, 561–566, doi:10.5194/npg-11-561-2004.

57. Leise, T. L.; Harrington, M. E. Wavelet-based time series analysis of Circadian rhythms. *J. Biol. Rhythms* **2011**, *26*, 454–463, doi:10.1177/0748730411416330.

58. Leopold, L. B.; Maddock, T. J. The Hydraulic Geomtry of Stream Channels and Some Physiographic Implications. *Geol. Surv. Prof. Pap. 252* **1953**, 57.

59. Bierman, P. R.; Montgomery, D. R. *Key Concepts in Geomorphology*; -, Ed.; 1st ed.; W.H.Freeman & Co Ltd: New York, 2014; Vol.; ISBN 9781429238601.

60. Calero Quesada, M. C.; García-Lafuente, J.; Garel, E.; Delgado Cabello, J.; Martins, F.; Moreno-Navas, J. Effects of tidal and river discharge forcings on tidal propagation along the Guadiana Estuary. *J. Sea Res.* **2019**, *146*, 1–13, doi:10.1016/j.seares.2019.01.006.

61. Soltaniasl, M.; Kawanisi, K.; Yano, J.; Ishikawa, K. Variability in salt flux and water circulation in Ota River Estuary , Japan. **2013**, *6*, 283–295, doi:10.3882/j.issn.1674-2370.2013.03.005.

62. Donnell, B. P.; Letter, J. V.; McAnally, W. H. *Users Guide to RMA2 WES Version 4.5*; New York, 2006;

63. Lippa, S. B. Hydrodynamic modeling of anthropogenic stress in a shallow microtidal estuary: Itajuru channel, Brazil, University of Toronto, 2006.

64. Danial, M. M.; Kawanisi, K.; Motlagh, M. B.; Al Sawaf, M. B.; Wakabayashi, T. Investigation of Flow Velocity and Salinity Behaviour in Ota River Estuary Using Acoustic Tomography Method and Numerical Modeling. *J. Japan Soc. Civ. Eng. Ser. B1 (Hydraulic Eng.* **2017**, *73*, I_1033-I_1038, doi:10.2208/jscejhe.73.i_1033.